

Evidence of high-mass star formation through multi-scale mass accretion in hub-filament-system clouds

Hong-Li Liu,^{*1} Anandmayee Tej,^{*2} Tie Liu,^{*3,4} Patricio Sanhueza,^{5,6} Shengli Qin,¹ Jinhua He,^{7,8,9} Paul F. Goldsmith,¹⁰ Guido Garay,⁹ Sirong Pan,¹ Kaho Morii,^{5,11} Shanghuo Li,¹² Amelia Stutz,^{13,14} Ken'ichi Tatematsu,⁵ Feng-Wei Xu,^{15,16} Leonardo Bronfman,⁹ Anindya Saha,² Namitha Issac,¹⁷ Tapas Baug,¹⁸ L. Viktor Toth,¹⁹ Lokesh Dewangan,²⁰ Ke Wang,^{15,16} Jianwen Zhou,²¹ Chang Won Lee,^{22,23} Dongting Yang,¹ Anxu Luo,¹ Xianjin Shen,¹ Yong Zhang,²⁴ Yue-Fang Wu,^{15,16} Zhiyuan Ren,²¹ Xun-Chuan Liu,³ Archana Soam,²⁵ Siju Zhang,^{15,16} Qiu-Yi Luo,³

Affiliations are listed at the end of the paper

Accepted 2023 January 3; Received 2022 December 6; in original form 2022 September 13

ABSTRACT

We present a statistical study of a sample of 17 hub-filament-system (HFS) clouds of high-mass star formation using high-angular resolution ($\sim 1\text{--}2''$) ALMA 1.3 mm and 3 mm continuum data. The sample includes 8 infrared (IR)-dark and 9 IR-bright types, which correspond to an evolutionary sequence from the IR-dark to IR-bright stage. The central massive clumps and their associated most massive cores are observed to follow a trend of increasing mass (M) and mass surface density (Σ) with evolution from IR-dark to IR-bright stage. In addition, a mass-segregated cluster of young stellar objects (YSOs) are revealed in both IR-dark and IR-bright HFSs with massive YSOs located in the hub and the population of low-mass YSOs distributed over larger areas. Moreover, outflow feedback in all HFSs are found to escape preferentially through the inter-filamentary diffuse cavities, suggesting that outflows would render a limited effect on the disruption of the HFSs and ongoing high-mass star formation therein. From the above observations, we suggest that high-mass star formation in the HFSs can be described by a multi-scale mass accretion/transfer scenario, from hub-composing filaments through clumps down to cores, that can naturally lead to a mass-segregated cluster of stars.

Key words: stars: formation – stars: massive; ISM: individual objects: hub filament system; ISM: clouds.

1 INTRODUCTION

High-mass stars are fundamental components of the universe, significantly impacting a multitude of astrophysical processes, for instance, the structure and evolution of the universe and its constituents (e.g., Larson 2003). Understanding how high-mass stars form has therefore long been an active area of astrophysical research (e.g., Motte, Bontemps, & Louvet 2018). It is generally accepted that high-mass stars form in clusters probably as a result of the hierarchical, multi-scale fragmentation process from clouds, through filaments, clumps and cores, down to seeds of star formation (e.g., Zhang et al. 2009; Wang et al. 2011, 2014; Beuther et al. 2018; Yuan et al. 2018; Vázquez-Semadeni et al. 2019; Li et al. 2019, 2020b; Padoan et al. 2020; Kumar et al. 2020; Liu et al. 2022a,b; Hacar et al. 2022; Chevance et al. 2022). Under this paradigm, filaments as a “conveyor belt” play a critical role in transporting gas material between the scales above and below (e.g., Longmore et al. 2014; Vázquez-Semadeni et al. 2019; Padoan et al. 2020; Kumar et al. 2020).

Indeed, filaments have been observed to be ubiquitous in the interstellar medium (ISM), and the sites of star formation in both nearby

low-mass and distant high-mass star-forming clouds (e.g., André et al. 2010, 2019; Molinari et al. 2010; Stutz & Gould 2016; Guo et al. 2021; Yuan et al. 2021). Crisscrossing filaments result in a special web that can comprise of three or more filaments converging toward a central web node. Defined as hub-filament systems (HFSs), these web networks are considered as a unique category of filaments for star formation, especially for high-mass star formation (e.g., Myers 2009; Kumar et al. 2020). In the definition of HFS, the web node is defined as the hub while the associated individual filaments are defined as the hub-composing filaments. In general, the central hub has a lower aspect ratio but a higher column density, which are in contrast to the high aspect ratio and low column density observed in the hub-composing filaments (e.g., Myers 2009; Kumar et al. 2020).

The hierarchical density structure discussed above can promote high-mass star formation. This is supported by several observational studies that include both single dish and interferometric observations from the far-infrared (IR) to millimeter regime (e.g., Schneider et al. 2012; Liu et al. 2012; Peretto et al. 2013; Williams et al. 2018; Yuan et al. 2018; Issac et al. 2019; Kumar et al. 2020; Anderson et al. 2021; Beltrán et al. 2022; Liu et al. 2022a,b; Sanhueza et al. 2021; Saha et al. 2022; Zhou et al. 2022; Thomasson et al. 2022). These studies reveal that young massive stellar clusters appear in HFSs with the high-mass stars being preferentially formed in the hubs.

* E-mail: hongliliu2012@gmail.com; tej@iist.ac.in; liutie@shao.ac.cn

Longitudinal gas flows along the hub-composing filaments, which are observed in several HFSs to converge toward the hub at typical flow rates of $\sim 10^{-4}$ – $10^{-3} M_{\odot} \text{ yr}^{-1}$, have been demonstrated to account for the required mass accretion (e.g., Yuan et al. 2018; Chen et al. 2019; Treviño-Morales et al. 2019; Liu et al. 2022a).

The above scenario advocates for further detailed observational studies of HFSs from the perspective of high-mass star formation and for the development of theoretical models. For instance, the latest-generation models such as “global hierarchical collapse” (GHC, Vázquez-Semadeni et al. 2019) and “inertial-inflow” (I2, Padoan et al. 2020), which in terms of the accretion process could be complementary to the two proposed competing theories of “turbulent core accretion” (McKee & Tan 2003) and “competitive accretion” (Bonnell et al. 2001). The merits of these latest-generation models can be attributed to the envisioned multi-scale gas accretion, from clouds to the seeds of star formation, which was proposed in earlier times as “clump-fed” accretion in simulations of Wang et al. (2010), but not fully developed to the cloud scales due to the computation limitation at that time. In addition, the HFSs are often reproduced to be a common signature in the multi-scale accretion models as the preferential system of cluster and high-mass star formation. However, the major driver of multi-scale gas accretion (e.g., gravity, and/or turbulence) is predicted to be different in different models (e.g., Liu et al. 2022b). This is inferred from our previous ALMA observations, at $\sim 2''$ resolution, toward a well-studied, high-mass star-forming filamentary IRDC, G034.43+00.24 (e.g., Sanhueza et al. 2010; Sakai et al. 2013; Foster et al. 2014; Liu et al. 2020, G34 hereafter). G34 can be regarded as an HFS with the hub located at the MM1 clump (see Fig. 1 of Liu et al. 2022a,b). Our investigations have revealed multi-scale accretion process from cloud down to the seeds of star formation and the scale-dependent nature of gas kinematics of the multi-scale, hierarchical density structures. Interpreting our results in the framework of both GHC and I2 models, we conclude that the scale-dependent combined effect of turbulence and gravity is essential to explain the multi-scale, dynamical accretion process responsible for high-mass star formation in G34.

In this paper, we aim to carry out a statistical study of a sample of 17 high-mass star forming HFSs using high-angular resolution (~ 1 – $2''$) ALMA continuum data. The sample was selected particularly to contain two different infrared (IR) characteristics (i.e., 8 IR-dark and 9 IR-bright objects) since these two IR types can represent two different evolutionary stages (see Sect. 2.1). The purpose of this study is to gain insights into high-mass star formation scenarios in HFS clouds by analysing the hierarchical structures of the HFSs as a function of evolution of high-mass star formation. The paper is organised as follows: Sect. 2 briefly describes the selection of the HFS sample and the ALMA data used, Sect. 3 presents analysis on the hierarchical structures of the HFSs (i.e., clouds, clumps, and cores), star formation therein, and the effect of outflow feedback on star formation. Sect. 4 discusses the multi-scale accretion scenario, from the core through clump up to the cloud scales, and Sect. 5 gives a comprehensive summary of the results obtained.

2 SAMPLE AND ALMA DATA

2.1 Sample

The sample investigated here consists of 17 HFS clouds selected from the ASHES (The ALMA Survey of 70 μm Dark High-mass Clumps in Early Stages; Sanhueza et al. 2019; Li et al. 2020; Sabatini et al. 2022) and the ATOMS (ALMA Three-millimeter Observations of Massive Star-forming regions; Liu et al. (2020a,b, 2021))

surveys. The selection is based on their morphological appearance in the Spitzer 8 μm image (see Fig. 1). The selected HFS cloud is required to be globally seen as an HFS morphology in 8 μm emission with at least three hub-composing filaments intersecting at the central hub (see Fig. 1). The hub-composing filaments appear as elongated dark lanes against bright 8 μm background emission. With the matching angular resolution (i.e., $2''$) as that of the ALMA data, the Spitzer image facilitates the ALMA analysis of the identified HFSs.

The selected HFSs are classified into 8 IR-dark and 9 IR-bright HFS clouds based on the lack or presence of IR emission in the central hubs. The IR-dark sample (i.e., HFSs 1–8) is from the ASHES survey where the hubs are identified as IR-dark clumps from 3.6 to 70 μm (Sanhueza et al. 2019). In contrast, the hubs of the IR-bright HFSs (i.e., HFSs 9–17), selected from the ATOMS survey, are bright in the same IR regime. This, in essence, is a reflection of the bolometric luminosity (L_{bol}) of the embedded young stellar objects (YSOs) in the hubs. Making a simple assumption, the L_{bol} of YSOs in these hubs is assumed to approximately represent that of their host HFSs (see Table 1). While the absence of compact IR emission can qualify the central hubs of IR-dark HFSs as prestellar candidates, being 70 μm dark does not always imply absolute lack of star formation (e.g., Li et al. 2019, 2020; Morii et al. 2021; Tafuya et al. 2021; Sakai et al. 2022). Hence, the lack of YSOs here could also indicate a relatively quiescent star formation stage with very low bolometric luminosities (i.e., $L_{\text{bol}} \lesssim 300 L_{\odot}$, see Table 1). On the other hand, the central hubs of the IR-bright HFSs have high-luminosity ($L_{\text{bol}} \gtrsim 10^4 L_{\odot}$, see Table 1) IRAS sources typical of high-mass stars, thus suggesting an active star formation stage. Interestingly, even with the relatively limited sample of HFSs investigated in this study strikingly different regimes of $L_{\text{bol}}/M_{\text{clump}}$ ratios are seen for the IR-dark and IR-bright HFSs (see Sect. 3.1). This lends strong support to the inference that two different star-formation stages are probed with these two IR types.

The basic parameters (e.g., source name, distance, and luminosity) of the selected sample are listed in Table 1. They have a median distance of ~ 3.6 kpc in a range of ~ 1.3 – 5.4 kpc with the IR-dark HFSs (~ 3.9 kpc) being on average around 1.4 times farther than the IR-bright ones (~ 2.7 kpc). It is worth noting that the 9 IR-bright HFSs selected here have been reported by Zhou et al. (2022) as part of a statistical study to identify and study HFSs in a large sample of 146 active massive protoclusters based on the H^{13}CO^+ (1–0) line data from the same ATOMS survey. Among the sample studied by Zhou et al. (2022), these 9 IR-bright HFSs stand out in terms of the 8 μm appearance of their hub-composing filaments as elongated dark lanes.

Figure 1 presents an example of the large-scale appearance of the selected 17 HFSs studied here in the Spitzer 8 μm image. Overlaid in gray contours on the image is ATLASGAL 870 μm continuum representative of cold, dense dust thermal emission. The size of the images was adjusted to recover the complete presence of the global HFS appearance in 8 μm emission. As shown in the figure, the global HFS appearance can be identified for all 17 HFS clouds with the hub-composing filaments intersecting at the centrally located hub. The hub-composing filaments seen as elongated dark lanes at 8 μm have associated 870 μm dust emission representative of cold and dense material, indicating that the filaments are essentially high-density structures.

2.2 ALMA data

We made use of the combined 12m+7m continuum data from ASHES (project IDs: 2015.1.01539.S, PI: Patricio Sanhueza), and

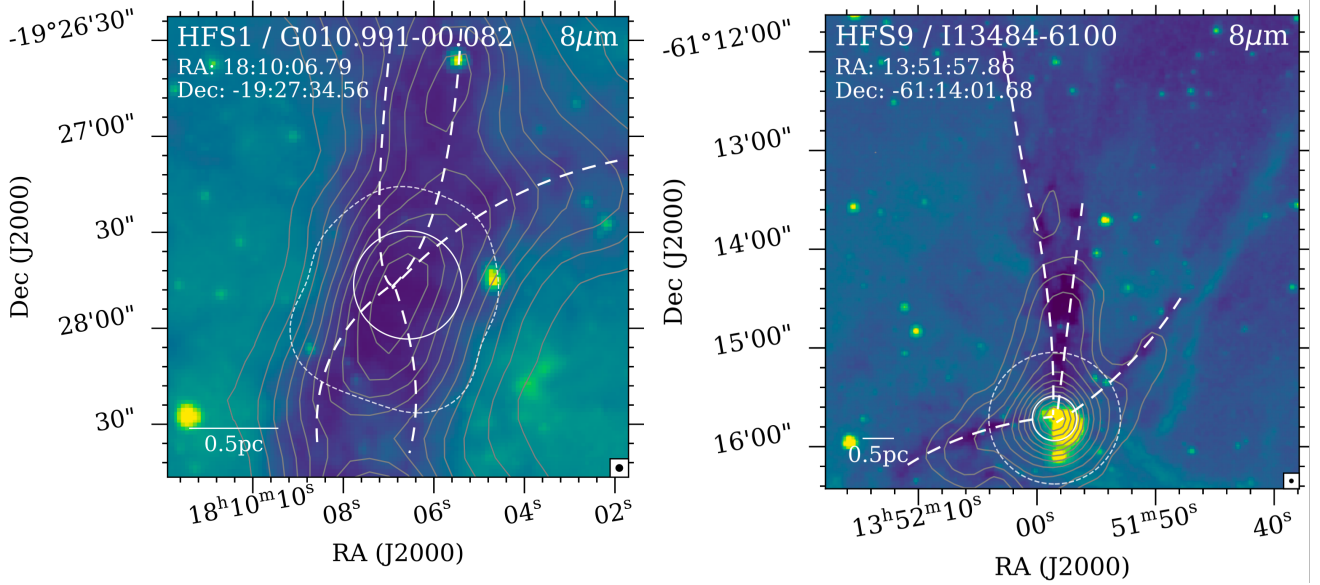


Figure 1. Images showing examples of the IR-dark (left) and bright (right) HFS clouds at Spitzer $8\mu\text{m}$. The contours represent $870\mu\text{m}$ dust continuum from the ATLASGAL survey (Schuller et al. 2009). The solid circles represent the compact dust clumps (Sect. 3.1). The dashed loop/circle demarcates the central subcloud field covered by our ALMA observations. The dashed curves identify the filamentary structures. The $8.0\mu\text{m}$ beam (i.e., $2''$) are shown at the bottom right-hand corner of the corresponding panel. The image size for each HFS is determined individually to recover the full view of its HFS morphology at $8\mu\text{m}$.

Table 1. Parameters of the HFSs and their central clumps.

HFS cloud ID	Alias	RA J2000	DEC J2000	d kpc	L_{bol} $\log(L_{\odot})$	T_{dust} K	$F_{870\mu\text{m}}^{\text{int.}}$ Jy	$M_{\text{clump}} M_{\odot}$	$\Sigma_{\text{clump}} \text{g cm}^{-2}$
1	G010.991-00.082	18:10:06.58	-19:27:46.44	3.7	1.7	12.0	1.94	355	0.38
2	G014.492-00.139	18:17:22.08	-16:24:59.40	3.9	2.5	13.0	3.89	685	0.73
3	G028.273-00.167	18:43:31.27	-4:13:18.48	5.1	1.6	12.0	1.05	365	0.39
4	G331.372-00.116	16:11:34.08	-51:34:56.28	5.4	1.6	14.0	0.90	266	0.28
5	G340.222-00.167	16:48:30.74	-45:11:04.56	4.0	1.6	15.0	1.07	155	0.17
6	G340.232-00.146	16:48:27.46	-45:09:48.24	3.9	1.1	14.0	1.16	179	0.19
7	G341.039-00.114	16:51:14.21	-44:31:24.24	3.6	1.8	14.3	1.21	153	0.16
8	G343.489-00.416	17:01:01.34	-42:48:07.92	2.9	0.8	10.3	1.04	156	0.17
9	I13484-6100	13:51:58.51	-61:15:42.84	5.4	4.8	31.8	4.10	600	0.64
10	I15394-5358	15:43:16.46	-54:07:15.24	1.8	3.7	34.0	29.69	482	0.51
11	I15520-5234	15:55:48.62	-52:43:05.88	2.6	5.1	32.2	38.82	733	0.78
12	I16272-4837	16:30:59.11	-48:43:53.40	2.9	4.3	23.1	17.64	748	0.80
13	I16351-4722	16:38:50.69	-47:27:58.68	3.0	4.9	30.4	25.43	649	0.69
14	I16424-4531	16:46:06.36	-45:36:44.64	2.6	3.9	24.6	6.70	153	0.16
15	I17016-4124	17:05:11.18	-41:29:05.28	1.4	5.3	32.0	51.16	975	1.04
16	I17233-3606	17:26:42.74	-36:09:18.00	1.3	4.6	29.9	123.33	201	0.21
17	I18507+0121	18:53:18.12	+1:25:24.24	3.7	3.5	22.7	13.34	882	0.94

Note: The distance d of the HFSs comes from Sanhueza et al. (2019) for HFSs 1–8, and Liu et al. (2021) for HFSs 9–17. The bolometric luminosity L_{bol} of the HFSs is approximately represented by that of their centrally located young stellar objects (YSOs, Bronfman, Nyman, & May 1996; Contreras et al. 2013; Liu et al. 2020a,b, 2021).

ATOMS (project ID: 2019.1.00685.S; PI: Tie Liu) surveys. Detailed discussion on the scientific goals, observing set-ups, and data reduction can be found in Sanhueza et al. (2019); Liu et al. (2020a,b, 2021). Briefly, the two surveys observed the central area of radius $\sim 31\text{--}39''$ of our selected HFSs (see the dashed loop in Fig. 1) in different observing modes at different wavelengths, i.e., the 1.3 mm mosaic mode for ASHES, and 3 mm pointing observing mode for ATOMS. In addition, the synthesized beams of the combined 12m+7m continuum data of the two surveys are different with

$\sim 1.2''$ for ASHES and $\sim 2.0''$ for ATOMS. However, the two surveys have similar field of views (FoVs, i.e., $\sim 62''$ for ASHES and $78''$ for ATOMS). Given their typical distances (see Sect. 2.1), the IR-dark and bright HFSs selected from the respective ASHES, and ATOMS surveys have very close linear-scale FoVs (i.e., $\sim 1.0\text{ pc}$ and $\sim 1.2\text{ pc}$, respectively). This rather close agreement of FoVs ensures detailed high-resolution analysis (e.g., for cores) over almost the same spatial scales for most of the HFSs studied here. The ASHES and ATOMS surveys have a maximum angular recoverable

scale of $19''$ and $60''$, respectively, for the combined data. Note that the different angular resolutions and maximum recoverable scales may lead to some observation biases to the properties of cores (e.g., mass), which will be discussed in Sect. 3.2.3. In addition, the typical sensitivities of the combined continuum data for ASHES and ATOMS are $\sim 0.1 \text{ mJy beam}^{-1}$ (Sanhueza et al. 2019) at 1.3 mm and $\sim 0.3 \text{ mJy beam}^{-1}$ at 3 mm (Liu et al. 2022a), respectively, which correspond to a mass sensitivity of $\sim 0.04 M_{\odot}$ (for a temperature of 15 K typical of IR-dark cases), and $\sim 1.2 M_{\odot}$ (for 25 K typical of IR-bright cases), respectively, at a typical distance of 3.6 kpc (see Sect. 3.1 for mass calculation).

3 RESULTS AND ANALYSIS

3.1 Clumps in the HFSs

Clumps are one of the characteristic hierarchical structures of the HFS clouds. From Fig. 1, one can see that each HFS has a dominant central clump. Generally, such density structures can be identified using several widely-used algorithms, such as *Dendrogram* and *CASA-imfit*. However, the use of these algorithms is limited by the intensity contrast of the clumps with respect to their natal clouds especially for the IR-dark HFSs studied here where the contrast is low (see Fig. 1). In these cases, the extracted clumps tend to have a large aspect ratio of > 3 (i.e., ratio of the major to minor axis) indicative of more than one entity within them. To avoid inaccurate clump identification for these low-contrast cases and to maintain uniformity, we define a circular aperture to enclose the enhanced $870 \mu\text{m}$ emission in the central area of both IR-dark and bright HFSs analysed here. From a careful scrutiny of the $870 \mu\text{m}$ maps of the entire sample, an optimum aperture with radius 0.25 pc is found suitable to encompass most of the $870 \mu\text{m}$ emission (see Fig. A1). Hence, we consider this as the radius of the clump, R_{clump} . Given this definition, the integrated flux ($F_{870\mu\text{m}}^{\text{int}}$) of the central clumps in all HFSs were extracted from the ATLASGAL $870 \mu\text{m}$ image. In addition, we retrieved the dust temperature (T_{dust}) of the clumps from Sanhueza et al. (2019) for those in the IR-dark HFSs and from Liu et al. (2020a) for those in the IR-bright HFSs. With the above parameters, the clump mass (M_{clump}) was computed following Eqs. B1–B2 of Liu et al. (2021). In the computation, we assumed the gas-to-dust mass ratio to be $R_{\text{gd}} = 100$, and the dust opacity per gram of dust to be $k_{870\mu\text{m}} = 1.78 \text{ cm}^2 \text{ g}^{-1}$, which corresponds to the opacity of dust grains with thin ice mantles at gas densities of 10^6 cm^{-3} (Ossenkopf & Henning 1994). The mass surface density (Σ_{clump}) of the clumps was derived from $\Sigma_{\text{clump}} = M_{\text{clump}}/(\pi R_{\text{clump}}^2)$. The derived parameters are listed in Table 1. According to Sanhueza et al. (2017, 2019), the uncertainty of both M_{clump} and Σ_{clump} could be about 50%, which accounts for the combined uncertainties from $k_{870\mu\text{m}}$ ($\sim 30\%$), R_{gd} ($\sim 20\%$), T_{d} ($\sim 20\%$), and the kinematic distance ($\sim 10\%$).

The central clumps have a median M_{clump} of $\sim 223 M_{\odot}$ in a range of $[153, 685] M_{\odot}$ in the IR-dark HFSs. For the IR-bright HFSs, the median M_{clump} is $\sim 649 M_{\odot}$ in a range of $[153, 975] M_{\odot}$. Σ_{clump} has a median value of 0.24 g cm^{-2} in a range of $[0.16, 0.73] \text{ g cm}^{-2}$ in the IR-dark HFSs, and 0.69 g cm^{-2} in a range of $[0.16, 1.04] \text{ g cm}^{-2}$ in the IR-bright HFSs. Overall, the estimated Σ_{clump} values in all HFSs studied here satisfy the empirical high-mass star formation threshold of $\Sigma_{\text{crit}} \geq 0.05 \text{ g cm}^{-2}$, which was derived from the mass-size relationship established using the ATLASGAL massive clumps containing high-mass star-forming signatures (e.g., methanol masers, and HII regions, Urquhart et al. 2014).

This provides evidence that the central clumps in both IR-dark and IR-bright HFSs are dense enough to form high-mass stars. Evidence of high-mass star formation in the IR-dark HFSs (i.e., HFSs 1–8) has been suggested in Sanhueza et al. (2019), while the same inference in the IR-bright HFSs (i.e., HFSs 9–17) is strengthened by their associated high luminosities of $L_{\text{bol}} \gtrsim 10^4 L_{\odot}$ (see Table 1).

To quantitatively describe the evolutionary stage of clumps that can represent the stage of their natal HFSs in terms of high-mass star formation, we consider the bolometric luminosity to mass ratio $L_{\text{bol}}/M_{\text{clump}}$, where the bolometric luminosity of each clump, L_{bol} , can be found in Table 1. This is approximately taken to be the luminosity of their centrally located YSOs (Bronfman, Nyman, & May 1996; Contreras et al. 2013; Liu et al. 2020a,b, 2021). This ratio is independent of distance, and has been widely used as an indicator of the evolutionary stage of clumps (e.g., Guzmán et al. 2015; Liu et al. 2021). The clumps in IR-dark and bright HFSs have a median $L_{\text{bol}}/M_{\text{clump}}$ value of $0.14 L_{\odot}/M_{\odot}$ in a range of $[0.04, 0.46] L_{\odot}/M_{\odot}$, and a median value of $105 L_{\odot}/M_{\odot}$ in a range of $[3.58, 204.62] L_{\odot}/M_{\odot}$, respectively. The ratio $L_{\text{bol}}/M_{\text{clump}}$ has been used as a diagnostic tool to probe the evolutionary stages of observed clumps (e.g., Urquhart et al. 2014; Giannetti et al. 2017; Elia et al. 2022). Based on the results discussed in these papers, values of $L_{\text{bol}}/M_{\text{clump}} \lesssim 2$ have been associated with a very early evolutionary phase of mass accretion and possibly the beginning of protostellar activity. Whereas, ratios between 2–40 are shown to represent a later evolutionary phase where the protostar grows in mass with continuing accretion reaching the zero age main sequence around $L_{\text{bol}}/M_{\text{clump}} \sim 10$. Beyond a ratio of $\gtrsim 40$, onset of radio emission with detection of hypercompact and UCHII regions. This strongly supports our conjecture that the ensemble of 8 IR-dark HFSs are at an earlier stage of high-mass star formation than that of the 9 IR-bright HFSs (see Sect. 2.1). Following this evolution, an overall increasing trend of both M_{clump} and Σ_{clump} can be found from the IR-dark ($223 M_{\odot}$ and 0.24 g cm^{-2}) to IR-bright ($649 M_{\odot}$ and 0.69 g cm^{-2}) stage of HFSs.

3.2 Cores in the HFSs

3.2.1 Core identification

The high-resolution ($1.2''$ – $2''$) ALMA continuum data, that correspond to linear scales 0.02 and 0.03 pc at the typical distances of the IR-dark and bright HFSs, respectively, enable the identification of compact cores where stars could form. A total of 224 compact cores in the 8 IR-dark HFSs have already been identified from ASHES 1.3 mm continuum by Sanhueza et al. (2019). Slightly different approaches have been implemented in Sanhueza et al. (2019) and Liu et al. (2021) to identify compact cores. While the former study used the *Dendrogram* algorithm, the later used a two-step process in which the initial identification was carried out using *Dendrogram* then followed by *CASA-imfit* to estimate the parameters. Examining the performance of both schemes (especially for the low-mass cores in the IR-dark HFSs) and to maintain uniformity, we use *Dendrogram* alone to extract cores in the 9 IR-bright HFSs from ATOMS 3 mm, combined 12m+7m continuum data. It is worth mentioning here that there are a suite of clump/core identification algorithms available (e.g., *Clumpfind* by Williams, de Geus, & Blitz 1994; *getsf* by Men'shchikov 2021) and *Dendrogram* is one such robust algorithm widely used in similar studies (e.g., Rosolowsky et al. 2008; Ginsburg et al. 2016; Offner et al. 2022). While a comparative study, which is beyond the focus of this paper, would help highlight the

Table 2. Parameters of cores in HFSs.

HFS cloud	Core ID	RA J2000	DEC J2000	R_{core} "	R_{core} AU	$F_{\text{cont}}^{\text{int}}$ mJy	M_{core} M_{\odot}	Σ_{core} g cm^{-2}	Assoc.
HFS9	ALMA1	13:51:58.35	-61:15:41.9	1.53	8242	56.63	289.9	12.07	1,2
HFS9	ALMA2	13:51:55.31	-61:16:05.4	1.57	8467	3.40	17.4	0.69	0
HFS9	ALMA3	13:52:00.74	-61:15:53.2	1.89	10190	4.70	24.1	0.66	0
HFS9	ALMA4	13:51:57.10	-61:15:51.0	1.69	9143	4.66	23.9	0.81	4
HFS9	ALMA5	13:51:58.09	-61:15:38.8	1.79	9639	3.43	17.6	0.53	0
HFS9	ALMA6	13:51:58.58	-61:15:33.9	0.98	5280	2.94	15.0	1.53	4
HFS9	ALMA7	13:51:57.87	-61:15:31.8	0.99	5323	2.86	14.6	1.46	4
HFS9	ALMA8	13:52:01.76	-61:15:25.0	1.16	6267	1.86	9.5	0.69	0
HFS9	ALMA9	13:51:57.56	-61:16:06.4	0.71	3851	0.86	4.4	0.84	4
HFS9	ALMA10	13:52:03.09	-61:15:53.5	0.69	3700	0.84	4.3	0.89	0
HFS9	ALMA11	13:51:58.29	-61:15:45.9	1.57	8496	1.93	9.9	0.39	4
HFS9	ALMA12	13:51:59.32	-61:15:41.1	1.64	8839	2.79	14.3	0.52	4
HFS10	ALMA1	15:43:18.94	-54:07:35.6	1.08	1962	8.69	5.1	3.71	2,4
HFS10	ALMA2	15:43:16.62	-54:07:14.8	2.80	5095	254.36	147.9	16.12	2,4
HFS10	ALMA3	15:43:18.36	-54:07:34.1	2.87	5213	17.49	10.2	1.06	0
HFS10	ALMA4	15:43:14.23	-54:07:27.7	1.13	2059	1.75	1.0	0.68	0
HFS10	ALMA5	15:43:16.91	-54:07:22.4	3.83	6973	7.55	4.4	0.26	0
HFS10	ALMA6	15:43:16.07	-54:07:10.9	2.13	3884	3.80	2.2	0.41	0
HFS10	ALMA7	15:43:17.15	-54:07:07.5	1.51	2739	2.58	1.5	0.57	0
HFS10	ALMA8	15:43:16.96	-54:06:59.4	1.14	2082	2.94	1.7	1.12	0
HFS10	ALMA9	15:43:15.76	-54:07:22.7	1.42	2577	1.81	1.1	0.45	0
HFS10	ALMA10	15:43:18.49	-54:07:17.7	0.70	1277	0.64	0.4	0.64	0
HFS11	ALMA1	15:55:48.46	-52:43:07.9	2.16	5723	190.43	234.7	20.27	1,3
HFS11	ALMA2	15:55:46.39	-52:43:23.5	1.07	2838	11.30	13.9	4.89	4
HFS11	ALMA3	15:55:47.93	-52:43:13.8	2.53	6693	32.84	40.5	2.56	0
HFS11	ALMA4	15:55:48.99	-52:43:12.0	1.02	2714	9.26	11.4	4.38	0
HFS11	ALMA5	15:55:48.87	-52:43:02.9	2.43	6430	28.63	35.3	2.41	0
HFS11	ALMA6	15:55:46.18	-52:43:00.7	0.67	1774	4.14	5.1	4.58	0
HFS12	ALMA1	16:30:58.82	-48:43:53.9	1.58	4601	156.58	234.3	31.30	1,2
HFS12	ALMA2	16:30:58.61	-48:43:57.4	2.44	7128	4.75	7.1	0.40	0
HFS12	ALMA3	16:30:59.26	-48:43:53.0	1.45	4219	2.41	3.6	0.57	0
HFS12	ALMA4	16:30:57.17	-48:43:54.4	1.18	3449	1.81	2.7	0.64	0
HFS12	ALMA5	16:30:57.37	-48:43:39.6	2.29	6685	22.57	33.8	2.14	2,4
HFS12	ALMA6	16:31:01.53	-48:44:05.2	0.73	2128	0.84	1.3	0.79	0
HFS12	ALMA7	16:30:59.32	-48:43:51.1	0.84	2439	1.19	1.8	0.85	0
HFS13	ALMA1	16:38:50.55	-47:28:01.8	2.34	7078	179.71	287.7	16.24	1,3
HFS13	ALMA2	16:38:51.68	-47:28:20.2	0.71	2155	1.47	2.4	1.43	4
HFS13	ALMA3	16:38:51.24	-47:28:13.9	1.13	3410	4.56	7.3	1.78	4
HFS13	ALMA4	16:38:50.06	-47:28:04.2	3.25	9812	11.91	19.1	0.56	4
HFS13	ALMA5	16:38:49.70	-47:27:55.7	0.82	2485	2.50	4.0	1.83	4
HFS13	ALMA6	16:38:50.61	-47:27:52.4	1.45	4377	3.73	6.0	0.88	0
HFS13	ALMA7	16:38:51.42	-47:27:48.1	1.24	3750	2.02	3.2	0.65	4
HFS13	ALMA8	16:38:51.77	-47:28:10.0	0.81	2432	1.20	1.9	0.92	4
HFS13	ALMA9	16:38:53.98	-47:28:02.8	0.66	2000	1.03	1.6	1.16	0
HFS13	ALMA10	16:38:51.60	-47:27:56.2	0.79	2397	1.21	1.9	0.95	4
HFS13	ALMA11	16:38:50.28	-47:27:47.3	0.83	2504	1.47	2.4	1.06	0
HFS14	ALMA1	16:46:06.08	-45:36:43.2	1.76	4625	28.41	34.5	4.56	1,2
HFS14	ALMA2	16:46:07.30	-45:36:40.9	1.16	3053	12.53	15.2	4.62	4
HFS14	ALMA3	16:46:06.88	-45:36:52.2	2.15	5639	8.07	9.8	0.87	4
HFS14	ALMA4	16:46:04.59	-45:36:53.9	1.09	2877	0.99	1.2	0.41	0
HFS14	ALMA5	16:46:05.99	-45:36:51.5	0.75	1966	1.63	2.0	1.45	4
HFS14	ALMA6	16:46:05.72	-45:36:48.3	0.99	2611	1.82	2.2	0.92	4
HFS14	ALMA7	16:46:05.04	-45:36:47.1	0.78	2059	0.52	0.6	0.42	4
HFS14	ALMA8	16:46:07.65	-45:36:39.1	1.36	3573	2.38	2.9	0.64	0
HFS14	ALMA9	16:46:08.43	-45:36:36.5	0.83	2181	0.75	0.9	0.54	0
HFS14	ALMA10	16:46:06.55	-45:36:39.9	3.16	8309	5.35	6.5	0.27	4
HFS15	ALMA1	17:05:11.15	-41:29:07.0	1.74	2380	271.70	89.5	44.69	3,4
HFS15	ALMA2	17:05:10.23	-41:29:33.0	1.07	1467	13.24	4.4	5.73	0
HFS15	ALMA3	17:05:09.52	-41:29:06.3	0.85	1167	9.58	3.2	6.55	0
HFS15	ALMA4	17:05:11.84	-41:29:01.3	0.95	1300	5.38	1.8	2.97	0
HFS15	ALMA5	17:05:09.57	-41:28:57.4	0.99	1351	5.62	1.9	2.87	0
HFS15	ALMA6	17:05:10.92	-41:28:47.3	1.71	2340	14.29	4.7	2.43	0
HFS15	ALMA7	17:05:09.40	-41:29:28.1	0.79	1078	4.47	1.5	3.59	0
HFS15	ALMA8	17:05:12.17	-41:29:08.5	0.80	1089	4.79	1.6	3.76	0
HFS16	ALMA1	17:26:42.56	-36:09:18.2	2.15	2885	623.10	196.4	66.75	1,3
HFS16	ALMA2	17:26:43.61	-36:09:17.1	1.50	2002	207.04	65.3	46.03	4
HFS16	ALMA3	17:26:42.96	-36:09:40.0	0.74	985	2.98	0.9	2.74	4
HFS16	ALMA4	17:26:40.26	-36:09:36.0	1.20	1611	5.06	1.6	1.74	0
HFS16	ALMA5	17:26:45.12	-36:09:19.8	0.71	948	3.38	1.1	3.35	0
HFS16	ALMA6	17:26:42.95	-36:09:13.3	2.28	3054	31.69	10.0	3.03	2,4
HFS16	ALMA7	17:26:43.59	-36:09:09.3	1.07	1436	10.35	3.3	4.47	4
HFS16	ALMA8	17:26:42.12	-36:09:20.7	1.12	1500	5.18	1.6	2.05	0
HFS16	ALMA9	17:26:43.38	-36:09:19.6	1.83	2449	16.63	5.2	2.47	0
HFS17	ALMA1	18:53:18.64	+1:24:46.5	1.03	3801	8.84	21.2	4.16	3,4
HFS17	ALMA2	18:53:18.07	+1:25:25.3	1.88	6952	158.09	379.9	22.23	1,2
HFS17	ALMA3	18:53:18.41	+1:24:54.2	1.23	4559	10.00	24.0	3.27	4
HFS17	ALMA4	18:53:18.33	+1:25:13.2	0.90	3338	4.41	10.6	2.69	4
HFS17	ALMA5	18:53:18.53	+1:25:18.1	0.87	3220	5.02	12.1	3.29	4
HFS17	ALMA6	18:53:18.23	+1:25:19.9	2.08	7680	3.84	9.2	0.44	2,4
HFS17	ALMA7	18:53:18.07	+1:25:30.1	2.15	7958	5.11	12.3	0.55	0
HFS17	ALMA8	18:53:18.66	+1:25:27.5	1.13	4193	5.00	12.0	1.93	4
HFS17	ALMA9	18:53:18.51	+1:25:37.3	2.11	7801	7.06	17.0	0.79	0
HFS17	ALMA10	18:53:18.75	+1:26:00.4	1.03	3824	5.05	12.1	2.35	4
HFS17	ALMA11	18:53:18.72	+1:24:44.1	1.15	4248	2.26	5.4	0.85	0
HFS17	ALMA12	18:53:18.43	+1:24:46.2	1.37	5070	2.12	5.1	0.56	0
HFS17	ALMA13	18:53:18.34	+1:25:09.8	1.15	4269	2.48	6.0	0.92	0

Note: This table includes only the parameters of cores in the nine IR-bright HFSs, while the same parameters of the cores in the eight IR-dark HFSs are referred to tables 3, and 4 of [Sanhueza et al. \(2019\)](#). $F_{\text{cont}}^{\text{int}}$ represents the integrated 3 mm continuum flux of the cores. Core association ranges from 0 to 4, where 0 = prestellar candidate, 1 = molecular outflow, 2 = hot core, 3 = compact HII region, and 4 = point-like $8/24 \mu\text{m}$ object.

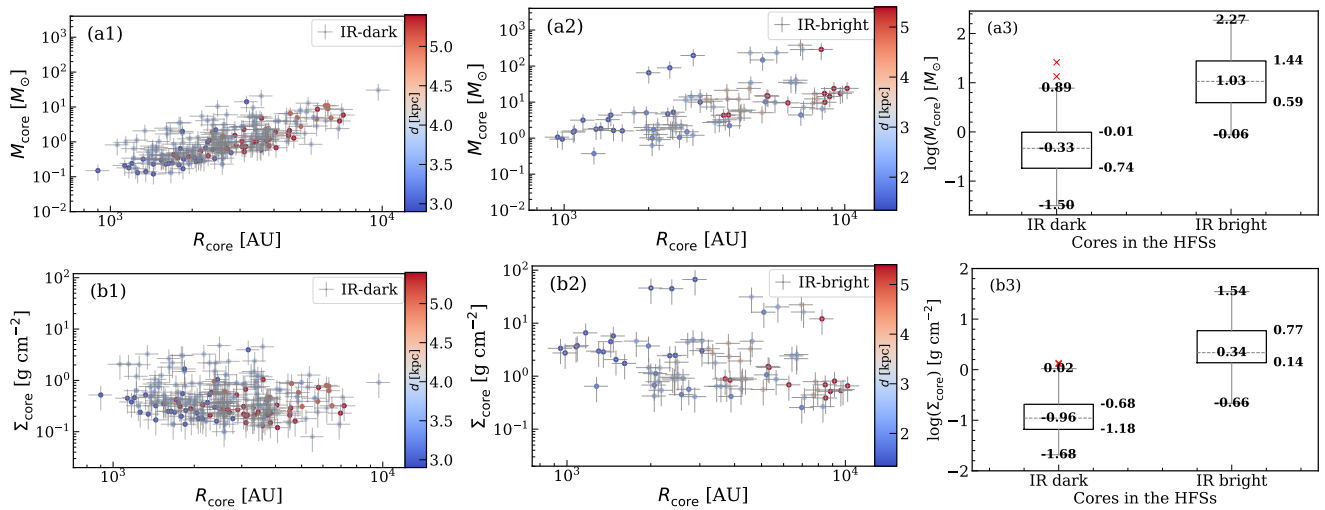


Figure 2. Panels (a1–a3): mass (M_{core}) distribution of cores. Panels a1, and a2 show the M_{core} distribution against the radius of cores located in the IR-dark, and IR-bright HFSs, respectively. The colors of dots in both panels represent the distances of the cores. Panel a3 displays a box-whisker plot summarising the M_{core} distribution of the cores in the two IR types of HFSs. Panels (b1–b3): same as Panels (a1–a3) but for the mass surface density (Σ_{core}) distribution. In the box-whisker plots, the numbers associated with the boxes from the top to bottom represent the upper quartile, median (inside the box), and lower quartile, respectively. The red crosses indicate the outliers outside 1.5 times the interquartile range either above the upper quartile or below the lower quartile.

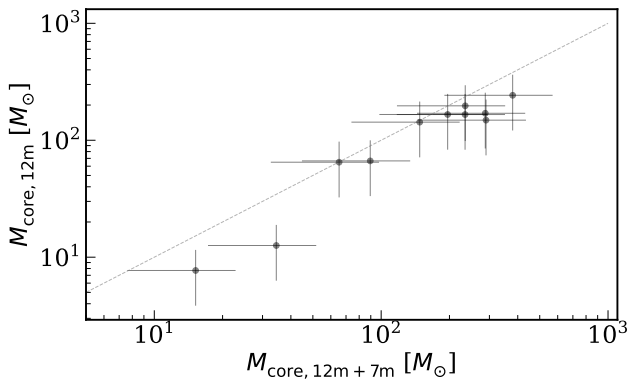


Figure 3. Comparison between determinations of the masses of the massive cores from the nine IR-bright HFSs, each having one clump. The core masses were derived first from the ATOMS 12m data alone, and second the combined 12m+7m data. The dashed line indicates equal mass from each set of observations.

nuances of each, the overall interpretation based on the retrieved parameters would remain the same.

Following Sanhueza et al. (2019), an intensity threshold of 2.5σ , a step of 1.0σ (the rms noise of the continuum data, see Sect. 2.2), and a minimum number of pixels equal to those contained in each synthesized beam (half of the beam considered in Sanhueza et al. 2019) were used as input parameters. The algorithm identifies the small structures, called “leaves”, which cannot further break up into smaller structures, and are thus defined here as cores. Finally, cores with integrated flux densities less than 4σ were excluded to avoid spurious identification, where 4σ was determined from the corresponding negative level (i.e., -4σ) within which the interferometric sidelobe effects cannot be ruled out. A total of 86 compact cores are obtained in the 9 IR-bright HFSs. The parameters retrieved from the *Dendrogram* analysis are listed in Table 2. These include the core coordinates, radius (R_{core}), and integrated flux ($F_{\text{cont}}^{\text{int}}$). The same

parameters for the compact cores in the 8 IR-dark HFSs are referred to Tables 3 and 4 of Sanhueza et al. (2019).

The number of the cores in the IR-bright HFSs found in this study is about four times greater than that reported in Liu et al. (2021) for the same regions. Apart from the slightly different parameter used, a possible reason is the use of the higher resolution 12m data for core extraction in Liu et al. (2021) as opposed to the combined 12m+7m data used here, which will be discussed below. Similar differences were noted by Sanhueza et al. (2019) where inclusion of more extended emission with the 7m array leads to detection of 20% greater number of cores.

3.2.2 Star-forming nature of cores

The star-forming activity in cores can be inferred from YSO signatures such as outflows, hot cores, compact HII regions. Li et al. (2020) provided the catalogues of CO and SiO outflows associated with the cores in the IR-dark HFSs while the association of hot cores and HII regions with the cores in the IR-bright HFSs are tabulated in Liu et al. (2021), who compiled these based on the detection of rich complex organic molecular lines, and $\text{H4}\alpha$ line. Presence of point-like $24\mu\text{m}$ or slightly extended but compact $8\mu\text{m}$ sources, which are likely to be candidate YSOs and hence could be considered as signposts of star formation. These associations are listed in the last column of Table 2. In total, 112 out of 310 cores are protostellar ones associated with one or more star-forming signatures (see above). The remaining 198 cores without any of these signatures are treated here as prestellar candidates.

3.2.3 Derived parameters of cores

From the parameters (e.g., radius R_{core} , and integrated flux $F_{\text{cont}}^{\text{int}}$) of the cores derived from the *Dendrogram* analysis discussed in Sect. 3.2.1, other parameters such as mass and mass surface densities can be estimated. Cores without detectable star-forming signatures are roughly assigned the temperature of their natal clumps. For cores with associated star-forming signatures, the temperature

was assumed to be 50 K for those associated with outflows (Sanhueza et al. 2019), and 100 K for those associated either with hot cores or compact HII regions (Liu et al. 2021). The mass (M_{core}) and mass surface density (Σ_{core}) parameters of the cores were calculated following the same approach outlined in Sect. 3.1, where the dust opacities per gram of dust were adjusted to be $0.9 \text{ cm}^2 \text{ g}^{-1}$ for 1 mm and $0.2 \text{ cm}^2 \text{ g}^{-1}$ for 3 mm according to Ossenkopf & Henning (1994). The uncertainties of M_{core} and Σ_{core} are around $\sim 50\%$ (see Sect. 3.1). The derived physical parameters are listed in Table 2.

It is worth noting that for those five cores associated with compact HII regions (see Table 2) that lie in five of nine IR-bright HFSs (i.e., HFSs 11, 13, 15, 16, 17), the continuum flux of cores would have contribution from both dust thermal emission and free-free emission. The values tabulated have been subtracted for the free-free emission component. To estimate the contribution of free-free emission, we used the H40 α hydrogen recombination line observations under the assumption of local thermodynamical equilibrium and optically thin emission. The free-free emission intensity was estimated via the following relation (e.g., Motte et al. 2022):

$$S_{\text{ff}} = 1.43 \times 10^{-4} S_{\text{RRL}} \left[\frac{\nu}{\text{GHz}} \right]^{-1.1} \left[\frac{T_e}{\text{K}} \right]^{1.15} \left(1 + \frac{N_{\text{He}}}{N_{\text{H}}} \right)^{-1}, \quad (1)$$

where S_{RRL} is the integrated intensity of H40 α over its velocity extent; $\nu = 99.0 \text{ GHz}$ is the rest frequency of H40 α observed in the ATOMS data; and we assume the electron temperature of $T_e = 6000 \text{ K}$ as well as a relative abundance of helium to hydrogen of $N_{\text{He}}/N_{\text{H}} = 0.08$. We assume an upper limit of $T_e = 6000 \text{ K}$ to avoid over subtraction of free-free continuum for the small scale extracted cores (Liu et al. 2015). The above estimated free-free emission intensity was subsequently subtracted from the 3 mm continuum image to yield the dust continuum emission image.

Figure 2 (a–b) show the distribution of M_{core} and Σ_{core} as a function of R_{core} for the cores in both IR-dark and bright HFSs. The colors in dots in the figure indicate the distance distribution. The cores in both IR types of HFSs have a similar radius range of $[0.9, 10] \times 10^3 \text{ AU}$, with an average radius ratio of ~ 1.4 of cores in the IR-dark HFSs to those in the IR-bright HFSs. As suggested by Luvet et al. 2021, this can be understood since the similar typical spatial resolutions of the ALMA observations toward the two IR-type HFSs can yield the close derived sizes of the extracted cores.

Considering the median values of the mass and mass surface density in the IR-bright HFSs ($5.7 M_{\odot}$ and 1.4 g cm^{-2}) and the IR-dark HFSs ($1.0 M_{\odot}$ and 0.4 g cm^{-2}), it is seen that the mass and mass surface density is higher by factors of 6 and 3, respectively in the IR-bright HFSs (Fig. 2 c). From Fig. 2 (a–b), this difference can be seen to be independent of the source distance. Instead, it could be in part a result of the observation bias caused by the different maximum recoverable scales (MRS) in the ASHES ($\sim 20''$) and ATOMS ($\sim 60''$) combined 12m+7m data. As suggested in Sanhueza et al. (2019), the higher MRS of the ATOMS combined data could intrinsically lead to higher fluxes and thus flux-derived parameters (e.g., mass and mass surface densities) of cores. Different mass sensitivity of the surveys could also contribute since in the higher sensitivity ASHES data, more low-mass cores are detected. However, it is worth noting that this observation bias could not affect significantly the most massive cores (i.e., nine cores with the highest M_{core} and Σ_{core} values in panels a–b), as can be seen from Fig. 3. Hence, in the analysis that follows, we focus on the most massive cores in the IR-bright sample of HFSs. In Fig. 3, we compare the masses estimated from the ATOMS 12m continuum data alone with a MRS of $\sim 18''$ (similar to the MRS of the ASHES data) with that derived from the 12m+7m combined data having a MRS of $\sim 60''$.

From this comparison, we estimate a nominal factor of ~ 1.3 on average higher mass estimates for the cores extracted in the IR-bright HFSs using ATOMS 12m+7m data. As is also seen in the figure, the most massive cores in the IR-bright HFSs can be clearly distinguished from the majority of low mass cores in the distributions of both M_{core} and Σ_{core} (see Fig. 2 a2 and b2). This trend could be either a consequence of the limited HFS sample investigated here or the evolutionary phase of the IR-bright HFSs, the latter being related to their preferred central location and sufficiently long accretion history. Certainly, larger sample of such IR-dark and IR-bright HFSs are required to examine the above possibilities.

3.3 YSOs in the HFSs

Investigating the spatial distribution of associated YSOs helps in understanding star formation in HFSs. From the $24 \mu\text{m}$ point source catalogue of the Galactic plane from Spitzer/MIPSGAL (Gutermuth & Heyer 2015), we searched for point sources associated with the HFS sample studied here, and obtained their $24 \mu\text{m}$ photometric fluxes. Here, we have used different search areas depending on the spatial extent of the HFSs in the $8 \mu\text{m}$ image (i.e., image size in Fig. 1, $1.5' - 4.8'$). In addition to the catalogued sources, we identified ten bright, point-like sources in the $24 \mu\text{m}$ MIPSGAL images that were not included in the MIPSGAL point source catalogue. These were identified in the HFSs 9, 11, 13, 14, 15, 16, and 17. For these sources, the photometry was performed manually using appropriate circular annulus whose inner and outer radii can represent well the point-like source and its associated background.

Since the typical distance of the HFSs studied here is $\sim 3.6 \text{ kpc}$, some of the $24 \mu\text{m}$ point sources obtained above could be foreground/background stars along the line of sight of the HFSs. To alleviate this, we correlate the identified sources with Gaia EDR3 data within a radius of $2''$. The parallax distances of the Gaia-matched sources were subsequently calculated. As a rough approximation, we assume that the sources with distance estimates more than 10% of the nearest HFS's distance are foreground/background stars. It is to be noted that only a few sources were filtered out as foreground/background stars. Finally, 175 point sources that are likely associated with the HFSs studied here are retained for further analysis.

Furthermore, we classify the identified YSOs cross-matching (within $2''$ radius) using the SPICY catalogue that compiles $\sim 120,000$ Spitzer/IRAC candidate YSOs for the Inner Galactic Midplane (Kuhn et al. 2021). This catalogue contains five classes of YSOs, including Class I, Flat-spectrum, Class II, Class III, and ‘‘Uncertain’’ YSOs that cannot be placed in any of the above four classes. Class I YSOs are highly embedded protostars with the bolometric luminosity dominated by a spherical infalling envelope; Class II YSOs are young stars surrounded by a substantial accreting disk; Class III YSOs are young stars with most of their disk mass being dissipated. Flat spectrum YSOs are those in between Class I and Class II. From the above exercise, 122 of the 175 detected $24 \mu\text{m}$ sources are classified as YSOs (29 and 93 in the IR-dark and IR-bright HFSs, respectively) and 53 as ‘‘unknown’’ sources. To confirm the nature of the ‘‘unknown’’ sources requires detailed investigation of the photometric information over multiple wavelengths, which is beyond the scope of this work.

The YSO luminosity can be directly linked to the star-formation process, i.e., either low or high-mass star formation. In previous studies, the $24 \mu\text{m}$ photometric flux of both low and high-mass protostellar sources was found to correlate well with their bolometric luminosity (L_{bol} , e.g., Dunham et al. 2008; Ragan et al. 2012). Ap-

Table 3. Statistical number of outflows in HFSs.

HFS ID	N (outflow lobes)	Filament-aligned	Filament-not-aligned (%)
HFS1	5	2	3 (60)
HFS2	10	0	10 (100)
HFS3	3	0	3 (100)
HFS4	7	1	6 (86)
HFS5	–	–	– (–)
HFS6	2	0	2 (100)
HFS7	13	1	12 (92)
HFS8	3	0	3 (100)
HFS9	2	0	2 (100)
HFS10	2	0	2 (100)
HFS11	1	0	1 (100)
HFS12	2	0	2 (100)
HFS13	2	0	2 (100)
HFS14	2	0	2 (100)
HFS15	2	1	1 (50)
HFS16	2	0	2 (100)
HFS17	7	1	6 (80)

Note: The statistics was made from Li et al. (2020) and Baug et al. 2022 (under preparation).

plying this empirical correlation, we estimated the luminosities of the 175 candidate YSOs from their $24\ \mu\text{m}$ fluxes. Except for the one luminous YSO ($L_{\text{bol}} \sim 10^4 L_{\odot}$; see Fig. 6), the candidate YSOs in the IR-dark HFSs have low luminosities of $L_{\text{bol}} < 10^3 L_{\odot}$. Note that the location of the one luminous YSO is more than 1 pc from the central hub of HFS 3, and thus do not conflict with the classification of the host HFS as IR-dark type. In case of the IR-bright HFSs, the majority of the candidate YSOs are also found to have low luminosities though there are 12 high-luminosity sources found with $L_{\text{bol}} \sim [10^4, 10^5] L_{\odot}$. The presence of a significant population of high-luminosity YSOs in the IR-bright HFSs agrees well with their more evolved stage inferred earlier.

3.4 Effects of outflow feedback on star formation

The final stellar mass depends not only on the initial mass reservoir of the natal clump but also on the mass accretion from the hub-composing filaments. However, several observational studies (e.g., Schneider et al. 2020) and theoretical simulations have shown the profound influence of stellar and protostellar feedback processes like collimated jets and bipolar outflows (e.g., Wang et al. 2010; Offner & Chaban 2017; Guszejnov et al. 2020, 2021; Verliat et al. 2022), and radiative heating (e.g., Bate 2009, 2012; Krumholz & Thompson 2012; Hennebelle et al. 2020, 2022; Grudić et al. 2022) in inhibiting mass accretion. Hence, for the protostar to grow in mass requires the strong accretion inflow to be least impacted by the above feedback processes in the early stages. As discussed in Dale & Bonnell (2011); Kumar et al. (2020), ionizing radiation, stellar wind and ionizing gas (HII regions) are found to channel out through pre-existing, inter-filamentary voids without dispelling the natal clump or inhibiting the mass inflow through filaments. In this study, we focus on the influence of outflows since these are pronounced in our HFSs sample.

The protostar’s spin, and hence the orientation of the outflows, is inherited from the core scale where the angular momentum is hierarchically transferred from the natal cloud through the filament onto the star-forming core. Given that the large-scale filamentary inflow is either onto the short axes of the filament or along the long axis, the alignment of the outflows is expected to be either preferentially parallel or perpendicular to the filament. Anathpindika & Whitworth (2008) found observational evidence that outflows are preferentially aligned perpendicular to the filaments. In compari-

son, observational results presented by Davis et al. (2009) and more recently by Stephens et al. (2017); Baug et al. (2021) reveal no preferred outflow-filament orientation. Several other studies have shown that the rotation of the protostar could be independent of the parent filament (e.g., Tatematsu et al. 2016) or could evolve significantly during formation (e.g., Lee et al. 2016; Offner et al. 2016). The outflow-filament alignment has implication on the forming protocluster in HFSs. If the outflows run along the individual filaments, the filament-rooted longitudinal mass flows will be inhibited or halted which will significantly hinder the mass growth of young stars embedded in the central hubs (e.g., Wang et al. 2010).

To understand the potential effect of outflows on star formation in the HFSs studied here, we compiled the parameters (i.e., position, and orientation) of the associated outflows from Li et al. (2020) and Baug et al. (2022; under preparation). Li et al. (2020) have catalogued the CO and SiO outflows of the 8 IR-dark HFSs (i.e., HFSs 1–8) taken from the ASHES survey data at ~ 1.3 mm (see Sect. 2), while Baug et al. (2022) provide the HCO⁺ outflows of the 9 IR-bright HFSs (i.e., HFSs 9–17) taken from the ATOMS survey data at ~ 3 mm (see Sect. 2). As indicated in Table 3, we obtain 60 outflow lobes for all the HFSs investigated here, where 38 and 22 outflow lobes are associated with the IR-dark and IR-bright HFSs, respectively. Note that we have considered the individual lobes of outflows here instead of the entire outflow entities.

The location and orientation of the identified outflows are displayed in Fig. 4, where the red/blue arrows indicate the estimated orientation and extent of the red/blue-shifted lobes. As evident from the figure, most of the outflows have spatial extents smaller than the dimension of the host HFS subclouds (i.e., the central dense regions covered by ALMA observations). This result indicates that the outflows might have not escaped the dense regions of the HFSs in early stages of star formation. However, this result may be an observational consequence due to the lack of total power in the analysis made in the ASHES and ATOMS surveys. But, if the outflows can escape the dense regions of the HFSs, then their direction can be traced by extending the identified outflows. These are shown as white arrows in the figure.

The statistics of the outflows and their orientation are tabulated in Table 3. For HFS 5 there are no identifiable outflows while HFS 1 and 15 have 60%, and 50% of filament-aligned outflows, respectively. Except for these three HFSs, all the other HFSs have the majority of outflows (i.e., $\geq 86\%$) not aligned with the individual filaments. There are a couple of caveats in the above analysis which need to be highlighted here. Firstly, the outflow identifications in the two studies used here are probably incomplete due to the presence of multiple overlapping outflows which tend to occur in high-mass star formation regions. Secondly, projection effects would also influence the observed orientations. Last but not the least, one needs to study more number of HFSs-outflow systems to enable a more robust statistical investigation. Keeping the above caveats in mind, our results show that the observed outflows (1) do not preferentially align parallel or perpendicular to the filaments and (2) tend to be oriented toward the voids of the hub-composing filaments. This suggests that, similar to the effect of other feedback processes, outflows render a limited effect on filamentary mass inflow and thus on the mass growth of young stars being formed in the centrally located hubs.

Moreover, the inference obtained above agrees with the quantitative analysis of the related energies. For the IR-dark HFSs, Li et al. (2020) found that the outflow-induced turbulence cannot sustain the internal turbulence of the natal clumps as the outflow energy rate is around two orders of magnitude less than the turbulent en-

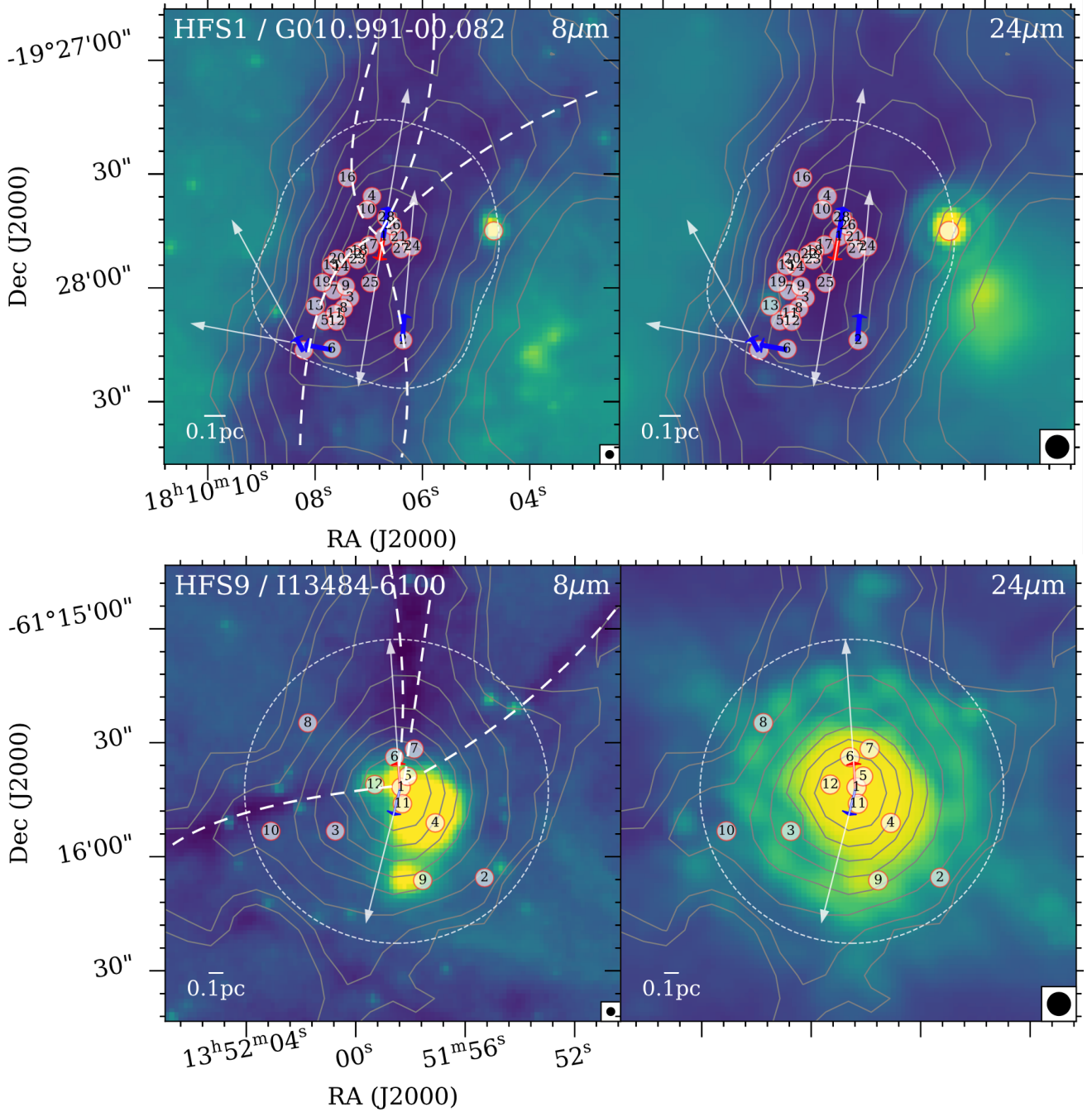


Figure 4. Zoom-in images of Spitzer $8\ \mu\text{m}$ and $24\ \mu\text{m}$ for the central regions of the IR-dark (in top row) and bright (in bottom row) HFS clouds. The contours represent $870\ \mu\text{m}$ dust continuum from the ATLASGAL survey (Schuller et al. 2009). The blue/red arrows are blue/red-shifted outflowing lobes identified by Li et al. (2020). They are purposely extended as white arrows for easy comparison of the relative orientation between the outflows and hub-composing filaments. The dashed loop delineates the central subcloud field covered by our ALMA observations. The red circles indicate the cores identified from the ALMA continuum data. The dashed curves identify the filamentary structures. The 8.0 and $24\ \mu\text{m}$ beams are shown at the bottom right-hand corner of the corresponding panel.

ergy dissipation rate. These authors also infer the outflow energy to be much smaller than the gravitational energy of the clumps. For the more evolved IR-bright HFSs investigated here, three of which (i.e., HFSs 11–13) were studied in terms of the outflow dynamics in Baug et al. (2021), they argued that the kinetic energy of outflows alone cannot balance the gravitational binding energy of the hosting clumps. Taken together, these results indicate the limited effect of

outflows on the destruction of their host HFSs in early stages and thus on the progress of star formation therein. However, as mentioned above, a larger sample and improved statistics on filament-outflow alignment is required to conclusively interpret simulations of outflow feedback (e.g., Wang et al. 2010; Offner & Chaban 2017; Guszejnov et al. 2020, 2021; Verliat et al. 2022) in the context of HFSs.

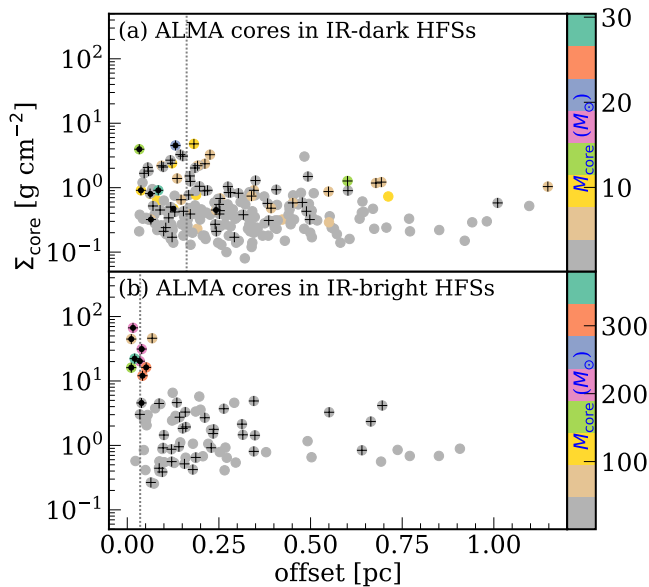


Figure 5. Distribution of mass surface density of cores in the HFSs against distance from the HFS centre. The colors in circles reflect the mass distribution of the cores. Panels (a) and (b) display the cores in the IR-dark, and IR-bright HFSs, respectively. In both panels, the protostellar cores are indicated in circles with inserted pluses while candidate starless cores are in empty circles. Circles with black dots inside are the centrally located most massive cores. The vertical dotted lines indicate the average distance weighted by the mass surface density of cores, i.e., 0.16 pc in panel a, and 0.04 pc in panel b.

4 DISCUSSION

4.1 Spatial distribution of cores and YSOs

Cores in the HFSs

Figure 5 shows the distribution of the mass surface density (Σ_{core}) of the cores as a function of the distance from the centre of the host HFSs. The centre is defined to be the position where the intensity of the $870\ \mu\text{m}$ emission peaks. Circles with inserted plus symbols distinguish the protostellar cores from that of the candidate starless ones. The centrally located most massive core of each HFS has an additional dot symbol included. Further, the plotted circles are colour-coded to represent the core mass (M_{core}) distribution. Several interesting trends can be deciphered from these plots and are discussed below.

The number of cores is more in the central region with only a sparse population seen beyond ~ 0.5 pc. The massive and dense cores in the IR-dark HFSs are located within ~ 0.25 pc, whereas, in IR-bright HFSs these are confined to the innermost region of ~ 0.05 pc. All nine centrally located most massive cores in IR-bright HFSs are forming high-mass stars as inferred from the associated high luminosities of $> 10^4 L_{\odot}$. This supports the scenario that in HFSs, the central areas of hubs are preferential sites for high-mass star formation where mass accretion occurs from the hub-composing filaments. The ideal location of such cores in IR-dark HFSs also qualifies them as potential high-mass star-forming cores.

The steep gradient seen in the spatial distribution of the most massive and dense cores towards the innermost region in IR-bright HFSs suggests a more centrally peaked clustering as opposed to the wider distribution observed in the IR-dark HFSs. That is, the spatial distribution of massive dense cores peaks at ~ 0.16 pc in IR-dark HFSs, but at ~ 0.04 pc in IR-bright HFSs, as indicated in the dotted lines in

the figure. These represent the average distance from the HFS centre weighted by the mass surface density over all the cores in each IR type of HFSs. The wider distribution of massive cores in the IR-dark hubs is in good agreement with the results of [Sanhueza et al. \(2019\)](#). These authors propose that cores in IR-dark HFSs originate from hierarchical subclustering rather than from centrally peaked clustering. The observed difference in the two IR types could suggest transformation to a centrally peaked clustering following the evolution of the host HFSs from the IR-dark to IR-bright stages.

Scarcity of high-mass prestellar cores (of $M_{\text{core}} \geq 30 M_{\odot}$ over the 0.1 pc scale, e.g., [Sanhueza et al. 2017, 2019](#)), the progenitors of high-mass stars, is observed in our sample of IR-dark HFSs. Here, none of the detected cores have masses greater than the threshold defined above. This allows us to conjecture that high-mass star formation could involve a dynamical, continuous mass accretion with evolution, which will be discussed further in Sect. 4.2. If we consider the prestellar cores in the IR-bright sample, only 11 ($\sim 13\%$ of cores) have mass estimates greater than $30 M_{\odot}$. For these to form high-mass stars, the same mass accretion process should ensue. However, the starless or prestellar nature of those cores needs to be confirmed through future higher-resolution observations with a more sensitive outflow tracer (e.g., CO 1–0),

YSOs in the HFS clouds

Figure 6 presents the distribution of bolometric luminosity (L_{bol}) of candidate YSOs against the distance from the centre of the host HFSs. In the IR-dark HFSs, the YSO's luminosity distribution is nearly constant at a low luminosity level (i.e., $\sim 100 L_{\odot}$) typical of low-mass protostars, regardless of the distance of the YSOs from the centre of the HFSs. Only one YSO with $L_{\text{bol}} \sim 10^4 L_{\odot}$, that is typical of high-mass protostars, is found at distance > 1 pc from the centre of the host HFSs. Furthermore, only two HFSs (i.e., HFSs 6, and 8) have identified YSOs (one each) within the hub-clump (i.e., central clump in the hub) region and their luminosities are low (i.e., $L_{\text{bol}} \lesssim 100 L_{\odot}$). In the case of the IR-bright HFSs, except for the three YSOs having $L_{\text{bol}} \sim 10^3\text{--}10^4 L_{\odot}$ located in a distance range of [1.6, 2.1] pc from the center of HFS 13, all of the YSOs show a decreasing trend in luminosity from high ($\gtrsim 10^4 L_{\odot}$) to low ($< 100 L_{\odot}$) luminosity values with the distance from the centre of the host HFSs up to ~ 2 pc, beyond which the YSOs display nearly constant low luminosity values. Note that given the not so high luminosities (i.e., $< 10^4 L_{\odot}$) of the above mentioned three luminous YSOs far from the centre of the host HFS 13, we assume that they could represent a cluster of intermediate and/or low-mass young stars instead of high-mass protostars, which agrees with the apparent multiplicity of these three YSOs seen at $8\ \mu\text{m}$ but not well resolved at $24\ \mu\text{m}$. In view of this, the observed decreasing trend suggests a luminosity/mass-segregated cluster formation picture in the IR-bright stage of HFSs, in which high-mass stars represented by high luminosities prefer to form in the central area of HFSs (i.e., the hub-clump region), while low-mass stars represented by low luminosities tend to form in the outskirts of HFSs up to several pc. In addition, the number of high-luminosity YSOs of $L_{\text{bol}} > 10^4 L_{\odot}$ found in IR-bright HFSs is larger (eleven; see star symbols in Fig. 6b) compared to the IR-dark HFSs where only one is detected. Moreover, almost each of the IR-bright HFSs has a corresponding high-luminosity YSO within the hub-clump region, in contrast to the absence of high-luminosity YSOs within the same region of the IR-dark HFSs. The above distribution of YSOs possibly implies an evolutionary sequence from a relatively quiescent, IR-dark phase to an active, IR-bright phase.

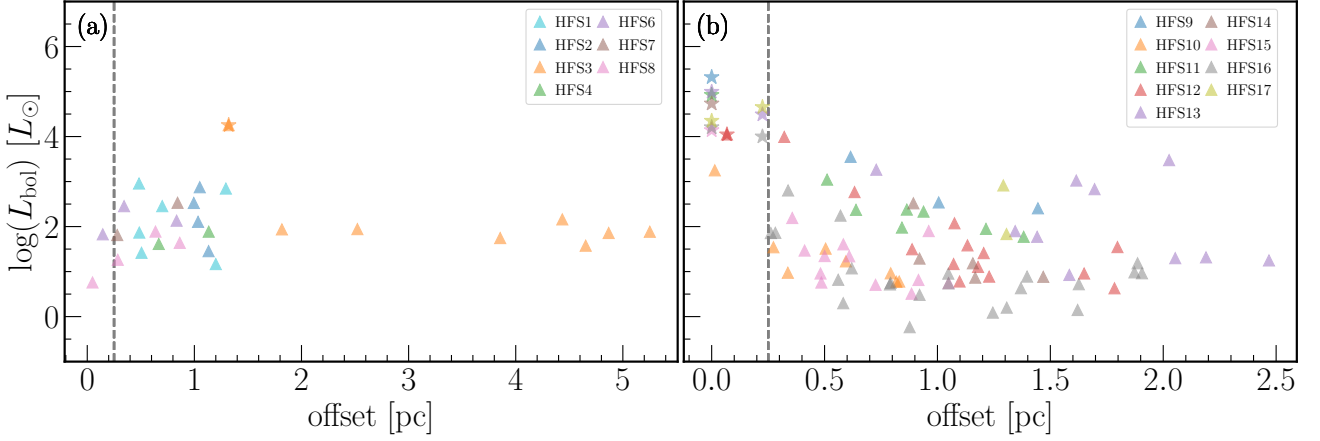


Figure 6. Luminosity of YSOs bright at $24\ \mu\text{m}$ associated with the IR-dark (panel a) and IR-bright HFSs (panel b) as a function of the distance from the HFS centre. The dashed lines indicate the typical size of the centrally-located clump for all HFSs, as defined in Fig. 5. Stars having luminosity above $10^4 L_{\odot}$ are shown as star symbols as opposed to those having luminosity below $10^4 L_{\odot}$ shown as triangle symbols.

4.2 Multi-scale mass transfer and high-mass star formation

Figure 7 presents the mass distribution of the central massive clumps of the HFSs (in panel a) and their embedded massive cores (in panel b) against the $L_{\text{bol}}/M_{\text{clump}}$ ratio of the clumps. The colors in circles in the figure represent the mass surface density of the sources. Note that, for this analysis, we have only considered the most massive cores since 1) they are (potential) sites of high-mass star formation, and 2) their mass and surface density estimates are not significantly affected by the observation bias caused by the different MRSs associated with the ASHES and ATOMS data (see Sect. 3.2.3). As shown in the figure, the IR-dark and IR-bright stages of HFSs can be well represented by the $L_{\text{bol}}/M_{\text{clump}}$ ratios of the clumps. The mass and mass surface density of the central clumps show a marginal increase of a factor of ~ 3 (on average) from the IR-dark to IR-bright stage. In comparison, for the embedded massive cores, the estimated values of the above parameters are enhanced by a factor of ~ 24 (on average) from the IR-dark to IR-bright stage. Additionally, as previously discussed (see Sect. 4.1), high-mass protostars (i.e., with $L_{\text{bol}} \gtrsim 10^4 L_{\odot}$) are only identified in the IR-bright HFSs. These results suggest that sufficient mass accumulation from the large-scale, hub-composing filaments is required for the central clumps in IR-dark HFSs to evolve to clumps with high-mass protostars in IR-bright HFSs. This process would continue till the hub-composing filaments are completely dispersed by stellar feedback (e.g., stellar winds, and ionization). Further, the associated massive cores accumulate the required mass from their natal clumps. Thus, a multi-scale mass accretion/transfer scenario unfolds in HFSs, where the mass accretion/transfer proceeds from the large-scale hub-composing filaments, through clumps, down to cores where high-mass stars finally form. Consistent with the observed trend, the mass and mass surface density of the clumps, and cores should be higher in the IR-bright stage of HFSs since the accretion timescales of these density structures are more extended in the more evolved stage as along as the large-scale hub-composing filaments contain sufficient gas material. This multi-scale mass accretion process has also been observed toward one of the HFSs studied here (i.e., HFS 17) in Liu et al. (2022a). These authors reveal the presence of the multi-scale mass accretion flows, i.e., accretion from clumps onto cores, and that from cores to embedded protostars.

The above results from a selected sub-sample of the ASHES

and ATOMS surveys agree well with the filament to cluster (i.e., F2C) evolutionary sequence discussed in a recent statistical study by Kumar et al. (2020). Based on a large sample of ~ 3700 candidate HFSs using far-infrared *Herschel* dust continuum maps at $70\text{--}500\ \mu\text{m}$ from the Hi-Gal survey, these authors propose four stages involved in the formation of high-mass stars in the context of HFSs. These are: I) formation of individual dense filaments by mechanisms such as cloud-cloud collisions, and compression from local turbulence; II) flow driven filaments overlap wherein intra-filamentary matter in the HFS cloud combine to form a hub with density amplification making them more conducive to star formation as compared to the filaments; III) formation of high-mass stars in the density amplified hub where the generated gravitational potential difference between the hub and the filaments can trigger and direct the filament-rooted longitudinal flows toward the centrally-located hub. IV) formation of “classical” (optically visible) HII regions in the hub along with a small embedded cluster of stars. In this stage, the radiation pressure and ionization feedback from the newly forming massive stars channel out of the hub through the inter-filamentary diffuse cavities. These four stages, where a multi-scale mass accretion/transfer process can be expected from hub-composing filaments through clumps (hubs) to cores (i.e., Stage II and III), finally lead to a mass-segregated embedded cluster with high-mass stars preferentially formed in the hub and low-mass stars in the hub-composing filaments.

From the observational study presented here, the IR-dark HFSs resemble Stage II, where the density-enhanced hub has formed and is in a relatively quiescent phase of star formation. Presence of low-luminosity YSOs outside the hub-clump region implies onset of low-mass star formation in the HFS cloud and/or individual filaments while the longitudinal flows continue to feed matter to the central hub which are devoid of high-luminosity sources. In comparison, the observational features seen in IR-bright HFSs are characteristic of Stage III. In this sample, in addition to a similar picture of low-mass star formation in the entire HFS cloud, a small, mass-segregated embedded cluster of YSOs (see Fig. 6b), in which high-luminosity YSOs ($\gtrsim 10^4 L_{\odot}$) typical of high-mass protostars are preferentially located in the hub-clump region. Interestingly, the orientation of outflows along the low density, inter-filamentary voids (see Sect. 3.4) also gives clues for channelling out radiation pressure

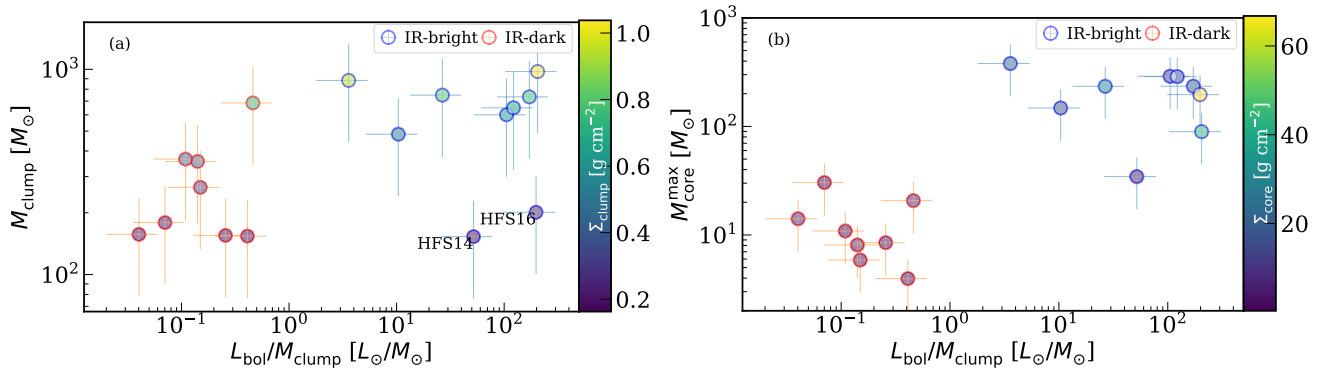


Figure 7. Mass distribution of the central massive clumps (panel a) and their embedded most massive cores (panel b) in the two IR types of HFS against the the $L_{\text{bol}}/M_{\text{clump}}$ ratio of the clumps. The color-coded circles reflect the mass surface density of the sources. The $L_{\text{bol}}/M_{\text{clump}}$ ratio of the clumps represent the evolutionary stage of high-mass star formation of the HFSs.

and ionization feedback in the next evolutionary stage (IV) of the classical HII regions.

Recent studies of molecular clouds found evidence for multi-scale hierarchical fragmentation cascade (i.e., from clouds, through filaments, clumps and cores, down to protostars, see e.g., [Elia et al. 2018](#); [Thomasson et al. 2022](#)) probably as a major vector of star formation. In conjunction with the latest theoretical models such as GHC ([Vázquez-Semadeni et al. 2019](#)) and I2 ([Padoan et al. 2020](#)), there seems to be a general consensus which can favor high-mass star formation in HFSs through a multi-scale mass accretion/transfer process that finally can lead to a mass-segregated cluster of stars. Notwithstanding the selection bias (see Sect. 3.2.3), one may consider the observed distinct mass distribution of the central massive clumps and their most massive cores as an evidence for the above processes in play in HFSs. Towards the above efforts and to put more robust constraints to theoretical models, companion papers (e.g., [Yang, D.T. et al. 2022](#), in prep.) are in the pipeline on high-resolution, multi-scale (i.e., from hub-composing filaments, clumps, to cores) kinematic and dynamical studies dedicated to the HFSs investigated here using the spectral line data from the same surveys. For example, the GHC and I2 models agree on gravity-driven mass-accretion on small scales (e.g., cores), however, they predict two distinct drivers on larger scales for the multi-scale mass accretion process. The former strongly favors a gravity-driven hierarchical mass accretion while the latter advocates for a turbulence-driven mass inflow/accretion, which can be disentangled with the multi-scale kinematic and dynamical studies.

5 SUMMARY AND CONCLUSIONS

We have presented a statistical study of a sample of 17 high-mass star formation HFSs using high-angular resolution ($\sim 1\text{--}2''$) ALMA 1.3 mm and 3 mm continuum data. The statistical results have helped shed light on the high-mass star formation scenario in HFSs. Our main results can be summarised as follows:

- The 17 HFSs are selected from the target lists of the ASHES 1.3 mm and ATOMS 3 mm surveys. They are identifiable in the Spitzer $8\ \mu\text{m}$ image with hub-composing filaments intersecting at the central hub. All the hub-composing filaments appear as elongated dark lanes in $8\ \mu\text{m}$ emission. Based on the different IR types of the hubs, the HFSs are divided into 8 IR-dark and 9 IR-bright HFSs. The IR-dark HFSs contain an IR-dark hub without detectable

IR emission shortward of $70\ \mu\text{m}$, while the IR-bright HFSs have an IR-bright hub with high-mass protostars in the same wavelength regime. The two IR types can represent an evolutionary sequence of high-mass star formation HFSs from the IR-dark to IR-bright stage.

- The 17 central massive clumps are identified in their natal HFSs from the available ATLASGAL $870\ \mu\text{m}$ continuum data. In addition, 310 embedded cores are extracted from the ALMA continuum data, including 224 from the IR-dark HFSs, and 86 from the IR-bright HFSs.

- The massive, dense cores in the two IR types of HFSs are predominantly distributed in the central hub-clump region of HFSs of radius $0.25\ \text{pc}$. For IR-dark HFSs, the cores peak within $\sim 0.16\ \text{pc}$ of the centre displaying a hierarchical sub-clustering mode. This transforms to a centrally-peaked clustering mode in IR-bright HFSs where the cores peak within $\sim 0.04\ \text{pc}$ of the centre.

- The central massive clumps and their associated most massive cores in HFSs show a trend of increasing mass and mass surface density with the evolution of HFSs from the IR-dark to IR-bright stage. This could be a natural result of the multi-scale mass accretion/transfer scenario in HFSs from the hub-composing filaments through clumps to cores.

- A total of 122 candidate YSOs associated with the 17 HFSs are retrieved from the combined catalogues of the archival Spitzer/MIPSGAL $24\ \mu\text{m}$ point sources and the Spitzer/IRAC candidate YSOs. Their stellar bolometric luminosities are estimated from the $24\ \mu\text{m}$ flux. From the spatial distributions of YSOs in the HFSs, we find the picture of a mass-segregated cluster of YSOs in which high-luminosity YSOs typical of high-mass protostars are preferentially located in the central hub-clump region, and surrounded by a population of low-luminosity YSOs typical of low-mass protostars in the entire HFS cloud extending to several parsecs.

- From qualitative analysis of the relative orientation between the outflow and hub-composing filaments in all the HFSs studied here, most of the outflows are found oriented toward the lower density inter-filamentary cavities. This suggests that outflow feedback would have a limited effect on the disruption of the HFS clouds and ongoing star formation therein.

From the observed facts of the trend on multi-scales (i.e., clumps and cores) of increasing mass and mass surface density with evolution from IR-dark to IR-bright stage, the mass-segregated cluster of YSOs, and the preferential escape directions of outflow feedback, we conclude that high-mass star formation in the HFSs can be described by a multi-scale mass accretion/transfer scenario, from hub-

composing filaments through clumps down to cores, that can naturally lead to a mass-segregated cluster of stars. To reveal the detailed physics related to the multi-scale accretion scenario requires further investigations, which will be carried out in our future multi-scale kinematic and dynamical studies dedicated to the HFSs investigated here using the high-resolution spectral line data from both ATOMS and ASHES surveys.

ACKNOWLEDGEMENTS

We thank the anonymous referee for comments and suggestions that greatly improved the quality of this paper. This work has been supported by the National Key R&D Program of China (No. 2022YFA1603101). H.-L. Liu is supported by National Natural Science Foundation of China (NSFC) through the grant No.12103045. T. Liu acknowledges the supports by NSFC through grants No.12073061 and No.12122307. PS was partially supported by a Grant-in-Aid for Scientific Research (KAKENHI Number 22H01271) of the Japan Society for the Promotion of Science (JSPS). S.-L. Qin is supported by NSFC under No.12033005. AS gratefully acknowledges support by the Fondecyt Regular (project code 1220610). This research was carried out in part at the Jet Propulsion Laboratory, which is operated by the California Institute of Technology under a contract with the National Aeronautics and Space Administration (80NM0018D0004). G.G., AS and L.B. gratefully acknowledges support by the ANID BASAL projects ACE210002 and FB210003. C.W.L. is supported by the Basic Science Research Program through the National Research Foundation of Korea (NRF) funded by the Ministry of Education, Science and Technology(NRF-2019R1A2C1010851), and by the Korea Astronomy and Space Science Institute grant funded by the Korea government (MSIT) (Project No. 2022-1-840-05). This work is supported by the international partnership program of Chinese Academy of Sciences through grant No.114231KYSB20200009, and Shanghai Pujiang Program 20PJ1415500. This paper makes use of the following ALMA data: ADS/JAO.ALMA#2019.1.00685.S and 2015.1.01539.S. ALMA is a partnership of ESO (representing its member states), NSF (USA), and NINS (Japan), together with NRC (Canada), MOST and ASIAA (Taiwan), and KASI (Republic of Korea), in cooperation with the Republic of Chile. The Joint ALMA Observatory is operated by ESO, AUI/NRAO, and NAOJ. This research made use of *astrodendro*, a Python package to compute dendrograms of Astronomical data (<http://www.dendrograms.org/>). This research made use of *Astropy*, a community-developed core Python package for Astronomy ([Astropy Collaboration et al. 2018](https://astropy.org/)).

DATA AVAILABILITY

The data underlying this article will be shared on reasonable request to the corresponding author.

REFERENCES

Anderson M., Peretto N., Ragan S. E., Rigby A. J., Avison A., Duarte-Cabral A., Fuller G. A., et al., 2021, *MNRAS*, 508, 2964. doi:10.1093/mnras/stab2674

André P., Men'shchikov A., Bontemps S., Könyves V., Motte F., Schneider N., Didelon P., et al., 2010, *A&A*, 518, L102. doi:10.1051/0004-6361/201014666

André P., Arzoumanian D., Könyves V., Shimajiri Y., Palmeirim P., 2019, *A&A*, 629, L4. doi:10.1051/0004-6361/201935915

Anathpindika S., Whitworth A. P., 2008, *A&A*, 487, 605. doi:10.1051/0004-6361:200810308

Astropy Collaboration, Price-Whelan A. M., Sipőcz B. M., Günther H. M., Lim P. L., Crawford S. M., Conseil S., et al., 2018, *AJ*, 156, 123. doi:10.3847/1538-3881/aabc4f

Bate M. R., 2009, *MNRAS*, 392, 1363. doi:10.1111/j.1365-2966.2008.14165.x

Bate M. R., 2012, *MNRAS*, 419, 3115. doi:10.1111/j.1365-2966.2011.19955.x

Baug T., Wang K., Liu T., Wu Y.-F., Li D., Zhang Q., Tang M., et al., 2021, *MNRAS*, 507, 4316. doi:10.1093/mnras/stab1902

Beltrán M. T., Rivilla V. M., Kumar M. S. N., Cesaroni R., Galli D., 2022, *A&A*, 660, L4. doi:10.1051/0004-6361/202243361

Beuther H., Mottram J. C., Ahmadi A., Bosco F., Linz H., Henning T., Klaassen P., et al., 2018, *A&A*, 617, A100. doi:10.1051/0004-6361/201833021

Bonnell I. A., Bate M. R., Clarke C. J., Pringle J. E., 2001, *MNRAS*, 323, 785. doi:10.1046/j.1365-8711.2001.04270.x

Bronfman L., Nyman L.-A., May J., 1996, *A&AS*, 115, 81

Chen H.-R. V., Zhang Q., Wright M. C. H., Busquet G., Lin Y., Liu H. B., Olguin F. A., et al., 2019, *ApJ*, 875, 24. doi:10.3847/1538-4357/ab0f3e

Chevance M., Krumholz M. R., McLeod A. F., Ostriker E. C., Rosolowsky E. W., Sternberg A., 2022, *arXiv*, arXiv:2203.09570

Contreras Y., Schuller F., Urquhart J. S., Csengeri T., Wyrowski F., Beuther H., Bontemps S., et al., 2013, *A&A*, 549, A45. doi:10.1051/0004-6361/201220155

Dale J. E., Bonnell I., 2011, *MNRAS*, 414, 321. doi:10.1111/j.1365-2966.2011.18392.x

Dunham M. M., Crapsi A., Evans N. J., Bourke T. L., Huard T. L., Myers P. C., Kauffmann J., 2008, *ApJS*, 179, 249. doi:10.1086/591085

Davis C. J., Froebrich D., Stanke T., Megeath S. T., Kumar M. S. N., Adamson A., Eisloffel J., et al., 2009, *A&A*, 496, 153. doi:10.1051/0004-6361:200811096

Elia D., Strafella F., Dib S., Schneider N., Hennebelle P., Pezzuto S., Molinari S., et al., 2018, *MNRAS*, 481, 509. doi:10.1093/mnras/sty2170

Elia D., Molinari S., Schisano E., Soler J. D., Merello M., Russeil D., Veneziani M., et al., 2022, *arXiv*, arXiv:2211.05573

Foster J. B., Arce H. G., Kassis M., Sanhueza P., Jackson J. M., Finn S. C., Offner S., et al., 2014, *ApJ*, 791, 108. doi:10.1088/0004-637X/791/2/108

Giannetti A., Leurini S., Wyrowski F., Urquhart J., Csengeri T., Menten K. M., König C., et al., 2017, *A&A*, 603, A33. doi:10.1051/0004-6361/201630048

Ginsburg A., Henkel C., Ao Y., Riquelme D., Kauffmann J., Pillai T., Mills E. A. C., et al., 2016, *A&A*, 586, A50. doi:10.1051/0004-6361/201526100

Goodman A. A., Pineda J. E., Schnee S. L., 2009, *ApJ*, 692, 91. doi:10.1088/0004-637X/692/1/91

Grudić M. Y., Guszejnov D., Offner S. S. R., Rosen A. L., Raju A. N., Faucher-Giguère C.-A., Hopkins P. F., 2022, *MNRAS*, 512, 216. doi:10.1093/mnras/stac526

Guszejnov D., Grudić M. Y., Hopkins P. F., Offner S. S. R., Faucher-Giguère C.-A., 2020, *MNRAS*, 496, 5072. doi:10.1093/mnras/staa1883

Guszejnov D., Grudić M. Y., Hopkins P. F., Offner S. S. R., Faucher-Giguère C.-A., 2021, *MNRAS*, 502, 3646. doi:10.1093/mnras/stab278

Guo W., Chen X., Feng J., Sun L., Wang C., Su Y., Sun Y., et al., 2021, *ApJ*, 921, 23. doi:10.3847/1538-4357/ac15fe

Gutermuth R. A., Heyer M., 2015, *AJ*, 149, 64. doi:10.1088/0004-6256/149/2/64

Guzmán A. E., Sanhueza P., Contreras Y., Smith H. A., Jackson J. M., Hoq S., Rathborne J. M., 2015, *ApJ*, 815, 130. doi:10.1088/0004-637X/815/2/130

Hacar A., Clark S., Heitsch F., Kainulainen J., Panopoulou G., Seifried D., Smith R., 2022, *arXiv*, arXiv:2203.09562

Hennebelle P., Commerçon B., Lee Y.-N., Chabrier G., 2020, *ApJ*, 904, 194. doi:10.3847/1538-4357/abfbab

Hennebelle P., Lebreuilly U., Colman T., Elia D., Fuller G., Leurini S., Nony T., et al., 2022, *arXiv*, arXiv:2210.12475

Issac N., Tej A., Liu T., Varricatt W., Vig S., Ishwara Chandra C. H., Schultheis M., 2019, *MNRAS*, 485, 1775. doi:10.1093/mnras/stz466

Krumholz M. R., Thompson T. A., 2012, *ApJ*, 760, 155. doi:10.1088/0004-637X/760/2/155

Kuhn M. A., de Souza R. S., Krone-Martins A., Castro-Ginard A., Ishida E. E. O., Povich M. S., Hillenbrand L. A., et al., 2021, *ApJS*, 254, 33.

- doi:10.3847/1538-4365/abe465
- Kumar M. S. N., Palmeirim P., Arzoumanian D., Inutsuka S. I., 2020, *A&A*, 642, A87. doi:10.1051/0004-6361/202038232
- Kumar M. S. N., Arzoumanian D., Men'shchikov A., Palmeirim P., Matsumura M., Inutsuka S., 2022, *A&A*, 658, A114. doi:10.1051/0004-6361/202140363
- Larson R. B., 2003, *RPPH*, 66, 1651. doi:10.1088/0034-4885/66/10/R03
- Lee K. I., Dunham M. M., Myers P. C., Arce H. G., Bourke T. L., Goodman A. A., Jørgensen J. K., et al., 2016, *ApJL*, 820, L2. doi:10.3847/2041-8205/820/1/L2
- Li S., Sanhueza P., Zhang Q., Nakamura F., Lu X., Wang J., Liu T., et al., 2020, *ApJ*, 903, 119. doi:10.3847/1538-4357/abb81f
- Li S., Zhang Q., Liu H. B., Beuther H., Palau A., Girart J. M., Smith H., et al., 2020, *ApJ*, 896, 110. doi:10.3847/1538-4357/ab84f1
- Li S., Zhang Q., Pillai T., Stephens I. W., Wang J., Li F., 2019, *ApJ*, 886, 130. doi:10.3847/1538-4357/ab464e
- Liu H. B., Quintana-Lacaci G., Wang K., Ho P. T. P., Li Z.-Y., Zhang Q., Zhang Z.-Y., 2012, *ApJ*, 745, 61. doi:10.1088/0004-637X/745/1/61
- Liu H. B., Galván-Madrid R., Jiménez-Serra I., Román-Zúñiga C., Zhang Q., Li Z., Chen H.-R., 2015, *ApJ*, 804, 37. doi:10.1088/0004-637X/804/1/37
- Liu H.-L., Sanhueza P., Liu T., Zavagno A., Tang X.-D., Wu Y., Zhang S., 2020, *ApJ*, 901, 31. doi:10.3847/1538-4357/abadfe
- Liu H.-L., Liu T., Evans N. J., Wang K., Garay G., Qin S.-L., Li S., et al., 2021, *MNRAS*, 505, 2801. doi:10.1093/mnras/stab1352
- Liu H.-L., Tej A., Liu T., Issac N., Saha A., Goldsmith P. F., Wang J.-Z., et al., 2022a, *MNRAS*, 510, 5009. doi:10.1093/mnras/stab2757
- Liu H.-L., Tej A., Liu T., Goldsmith P. F., Stutz A., Juvela M., Qin S.-L., et al., 2022b, *MNRAS*, 511, 4480. doi:10.1093/mnras/stac378
- Liu T., Evans N. J., Kim K.-T., Goldsmith P. F., Liu S.-Y., Zhang Q., Tatematsu K., et al., 2020a, *MNRAS*, 496, 2790. doi:10.1093/mnras/staa1577
- Liu T., Evans N. J., Kim K.-T., Goldsmith P. F., Liu S.-Y., Zhang Q., Tatematsu K., et al., 2020b, *MNRAS*, 496, 2821. doi:10.1093/mnras/staa1501
- Longmore S. N., Kruijssen J. M. D., Bastian N., Bally J., Rathborne J., Testi L., Stolte A., et al., 2014, *prpl.conf*, 291. doi:10.2458/azu.uapress.9780816531240-ch013
- Louvet F., Hennebelle P., Men'shchikov A., Didelon P., Ntormousi E., Motte F., 2021, *A&A*, 653, A157. doi:10.1051/0004-6361/202040053
- McKee C. F., Tan J. C., 2003, *ApJ*, 585, 850. doi:10.1086/346149
- Men'shchikov A., 2021, *A&A*, 649, A89. doi:10.1051/0004-6361/202039913
- Molinari S., Swinyard B., Bally J., Barlow M., Bernard J.-P., Martin P., Moore T., et al., 2010, *A&A*, 518, L100. doi:10.1051/0004-6361/201014659
- Morii K., Sanhueza P., Nakamura F., Jackson J. M., Li S., Beuther H., Zhang Q., et al., 2021, *ApJ*, 923, 147. doi:10.3847/1538-4357/ac2365
- Motte F., Bontemps S., Csengeri T., Pouteau Y., Louvet F., Stutz A. M., Cunningham N., et al., 2022, *A&A*, 662, A8. doi:10.1051/0004-6361/202141677
- Motte F., Bontemps S., Louvet F., 2018, *ARA&A*, 56, 41. doi:10.1146/annurev-astro-091916-055235
- Myers P. C., 2009, *ApJ*, 700, 1609. doi:10.1088/0004-637X/700/2/1609
- Offner S. S. R., Dunham M. M., Lee K. I., Arce H. G., Fielding D. B., 2016, *ApJL*, 827, L11. doi:10.3847/2041-8205/827/1/L11
- Offner S. S. R., Chaban J., 2017, *ApJ*, 847, 104. doi:10.3847/1538-4357/aa8996
- Offner S. S. R., Taylor J., Markey C., Chen H. H.-H., Pineda J. E., Goodman A. A., Burkert A., et al., 2022, *MNRAS*, 517, 885. doi:10.1093/mnras/stac2734
- Ossenkopf V., Henning T., 1994, *A&A*, 291, 943
- Padoan P., Pan L., Juvela M., Haugbølle T., Nordlund Å., 2020, *ApJ*, 900, 82. doi:10.3847/1538-4357/abaa47
- Peretto N., Fuller G. A., Duarte-Cabral A., Avison A., Hennebelle P., Pineda J. E., André P., et al., 2013, *A&A*, 555, A112. doi:10.1051/0004-6361/201321318
- Ragan S., Henning T., Krause O., Pitann J., Beuther H., Linz H., Tackenberg J., et al., 2012, *A&A*, 547, A49. doi:10.1051/0004-6361/201219232
- Rosolowsky E. W., Pineda J. E., Kauffmann J., Goodman A. A., 2008, *ApJ*, 679, 1338. doi:10.1086/587685
- Sabatini G., Bovino S., Sanhueza P., Morii K., Li S., Redaelli E., Zhang Q., et al., 2022, *ApJ*, 936, 80. doi:10.3847/1538-4357/ac83aa
- Sanhueza P., Garay G., Bronfman L., Mardones D., May J., Saito M., 2010, *ApJ*, 715, 18. doi:10.1088/0004-637X/715/1/18
- Sanhueza P., Jackson J. M., Zhang Q., Guzmán A. E., Lu X., Stephens I. W., Wang K., et al., 2017, *ApJ*, 841, 97. doi:10.3847/1538-4357/aa6ff8
- Sanhueza P., Contreras Y., Wu B., Jackson J. M., Guzmán A. E., Zhang Q., Li S., et al., 2019, *ApJ*, 886, 102. doi:10.3847/1538-4357/ab45e9
- Sanhueza P., Girart J. M., Padovani M., Galli D., Hull C. L. H., Zhang Q., Cortes P., et al., 2021, *ApJL*, 915, L10. doi:10.3847/2041-8213/ac081c
- Saha A., Tej A., Liu H.-L., Liu T., Issac N., Lee C. W., Garay G., et al., 2022, *MNRAS*, 516, 1983. doi:10.1093/mnras/stac2353
- Sakai T., Sakai N., Foster J. B., Sanhueza P., Jackson J. M., Kassis M., Furuya K., et al., 2013, *ApJL*, 775, L31. doi:10.1088/2041-8205/775/1/L31
- Sakai T., Sanhueza P., Furuya K., Tatematsu K., Li S., Aikawa Y., Lu X., et al., 2022, *ApJ*, 925, 144. doi:10.3847/1538-4357/ac3d2e
- Schneider N., Csengeri T., Hennemann M., Motte F., Didelon P., Federath C., Bontemps S., et al., 2012, *A&A*, 540, L11. doi:10.1051/0004-6361/201118566
- Schneider N., Simon R., Guevara C., Buchbender C., Higgins R. D., Okada Y., Stutzki J., et al., 2020, *PASP*, 132, 104301. doi:10.1088/1538-3873/aba840
- Schuller F., Menten K. M., Contreras Y., Wyrowski F., Schilke P., Bronfman L., Henning T., et al., 2009, *A&A*, 504, 415. doi:10.1051/0004-6361/200811568
- Stephens I. W., Dunham M. M., Myers P. C., Pokhrel R., Sadavoy S. I., Vorobyov E. I., Tobin J. J., et al., 2017, *ApJ*, 846, 16. doi:10.3847/1538-4357/aa8262
- Stutz A. M., Gould A., 2016, *A&A*, 590, A2. doi:10.1051/0004-6361/201527979
- Treviño-Morales S. P., Fuente A., Sánchez-Monge Á., Kainulainen J., Didelon P., Suri S., Schneider N., et al., 2019, *A&A*, 629, A81. doi:10.1051/0004-6361/201935260
- Tafoya D., Sanhueza P., Zhang Q., Li S., Guzmán A. E., Silva A., de la Fuente E., et al., 2021, *ApJ*, 913, 131. doi:10.3847/1538-4357/abf5da
- Tatematsu K., Ohashi S., Sanhueza P., Nguyen Luong Q., Umemoto T., Mizuno N., 2016, *PASJ*, 68, 24. doi:10.1093/pasj/psw002
- Thomasson B., Joncour I., Moraux E., Crespelle C., Motte F., Pouteau Y., Nony T., 2022, *A&A*, 665, A119. doi:10.1051/0004-6361/202243275
- Urquhart J. S., Moore T. J. T., Csengeri T., Wyrowski F., Schuller F., Hoare M. G., Lumsden S. L., et al., 2014, *MNRAS*, 443, 1555. doi:10.1093/mnras/stu1207
- Vázquez-Semadeni E., Palau A., Ballesteros-Paredes J., Gómez G. C., Zamora-Avilés M., 2019, *MNRAS*, 490, 3061. doi:10.1093/mnras/stz2736
- Verliat A., Hennebelle P., González M., Lee Y.-N., Geen S., 2022, *A&A*, 663, A6. doi:10.1051/0004-6361/202141765
- Wang P., Li Z.-Y., Abel T., Nakamura F., 2010, *ApJ*, 709, 27. doi:10.1088/0004-637X/709/1/27
- Wang K., Zhang Q., Wu Y., Zhang H., 2011, *ApJ*, 735, 64. doi:10.1088/0004-637X/735/1/64
- Wang K., Zhang Q., Testi L., van der Tak F., Wu Y., Zhang H., Pillai T., et al., 2014, *MNRAS*, 439, 3275. doi:10.1093/mnras/stu127
- Williams J. P., de Geus E. J., Blitz L., 1994, *ApJ*, 428, 693. doi:10.1086/174279
- Williams G. M., Peretto N., Avison A., Duarte-Cabral A., Fuller G. A., 2018, *A&A*, 613, A11. doi:10.1051/0004-6361/201731587
- Yuan J., Li J.-Z., Wu Y., Ellingsen S. P., Henkel C., Wang K., Liu T., et al., 2018, *ApJ*, 852, 12. doi:10.3847/1538-4357/aa9d40
- Yuan L., Yang J., Du F., Liu X., Zhang S., Lin Z., Sun J., et al., 2021, *ApJS*, 257, 51. doi:10.3847/1538-4365/ac242a
- Zhang Q., Wang Y., Pillai T., Rathborne J., 2009, *ApJ*, 696, 268. doi:10.1088/0004-637X/696/1/268
- Zhou J.-W., Liu T., Evans N. J., Garay G., Goldsmith P. F., Gómez G. C., Vázquez-Semadeni E., et al., 2022, *MNRAS*.tmp. doi:10.1093/mnras/stac1735

APPENDIX A: COMPLEMENTARY FIGURES

MS-12, N232, Moffett Field, CA 94035, USA

Author affiliations:

¹School of physics and astronomy, Yunnan University, Kunming, 650091, PR China

²Indian Institute of Space Science and Technology, Thiruvananthapuram 695 547, Kerala, India

³Shanghai Astronomical Observatory, Chinese Academy of Sciences, 80 Nandan Road, Shanghai 200030, Peoples Republic of China

⁴Key Laboratory for Research in Galaxies and Cosmology, Shanghai Astronomical Observatory, Chinese Academy of Sciences, 80 Nandan Road, Shanghai 200030, Peoples Republic of China

⁵National Astronomical Observatory of Japan, National Institutes of Natural Sciences, 2-21-1 Osawa, Mitaka, Tokyo 181-8588, Japan

⁶Department of Astronomical Science, The Graduate University for Advanced Studies, SOKENDAI, 2-21-1 Osawa, Mitaka, Tokyo 181-8588, Japan

⁷Yunnan Observatories, Chinese Academy of Sciences, 396 Yangfangwang, Guandu District, Kunming, 650216, China

⁸Chinese Academy of Sciences South America Center for Astronomy, National Astronomical Observatories, CAS, Beijing 100101, China

⁹Departamento de Astronomía, Universidad de Chile, Casilla 36-D, Santiago, Chile

¹⁰Jet Propulsion Laboratory, California Institute of Technology, 4800 Oak Grove Drive, Pasadena, CA 91109, USA

¹¹Department of Astronomy, Graduate School of Science, The University of Tokyo, 7-3-1 Hongo, Bunkyo-ku, Tokyo 113-0033, Japan

¹²Max Planck Institute for Astronomy, Knigstuhl 17, D-69117 Heidelberg, Germany

¹³Departamento de Astronomía, Universidad de Concepción, Av. Esteban Iturra s/n, Distrito Universitario, 160-C, Chile

¹⁴Max-Planck-Institute for Astronomy, Königstuhl 17, 69117 Heidelberg, Germany

¹⁵Kavli Institute for Astronomy and Astrophysics, Peking University, 5 Yiheyuan Road, Haidian District, Beijing 100871, People's Republic of China

¹⁶Department of Astronomy, Peking University, 100871, Beijing, People's Republic of China

¹⁷Indian Institute of Astrophysics, Koramangala II Block, Bangalore 560 034, India

¹⁸Satyendra Nath Bose National Centre for Basic Sciences, Block-JD, Sector-III, Salt Lake, Kolkata-700 106

¹⁹Eötvös Loránd University, Department of Astronomy, Pázmány Péter sétány 1/A, H-1117, Budapest, Hungary

²⁰Physical Research Laboratory, Navrangpura, Ahmedabad 380 009, India

²¹National Astronomical Observatories, Chinese Academy of Sciences, Beijing 100101, China

²²Korea Astronomy and Space Science Institute, 776 Daedeok-daero, Yuseong-gu, Daejeon 34055, Republic of Korea

²³University of Science and Technology, Korea (UST), 217 Gajeong-ro, Yuseong-gu, Daejeon 34113, Republic of Korea

²⁴School of Physics and Astronomy, Sun Yat-sen University, 2 Daxue Road, Zhuhai, Guangdong, 519082, People's Republic of China

²⁵SOFIA Science Centre, USRA, NASA Ames Research Centre,

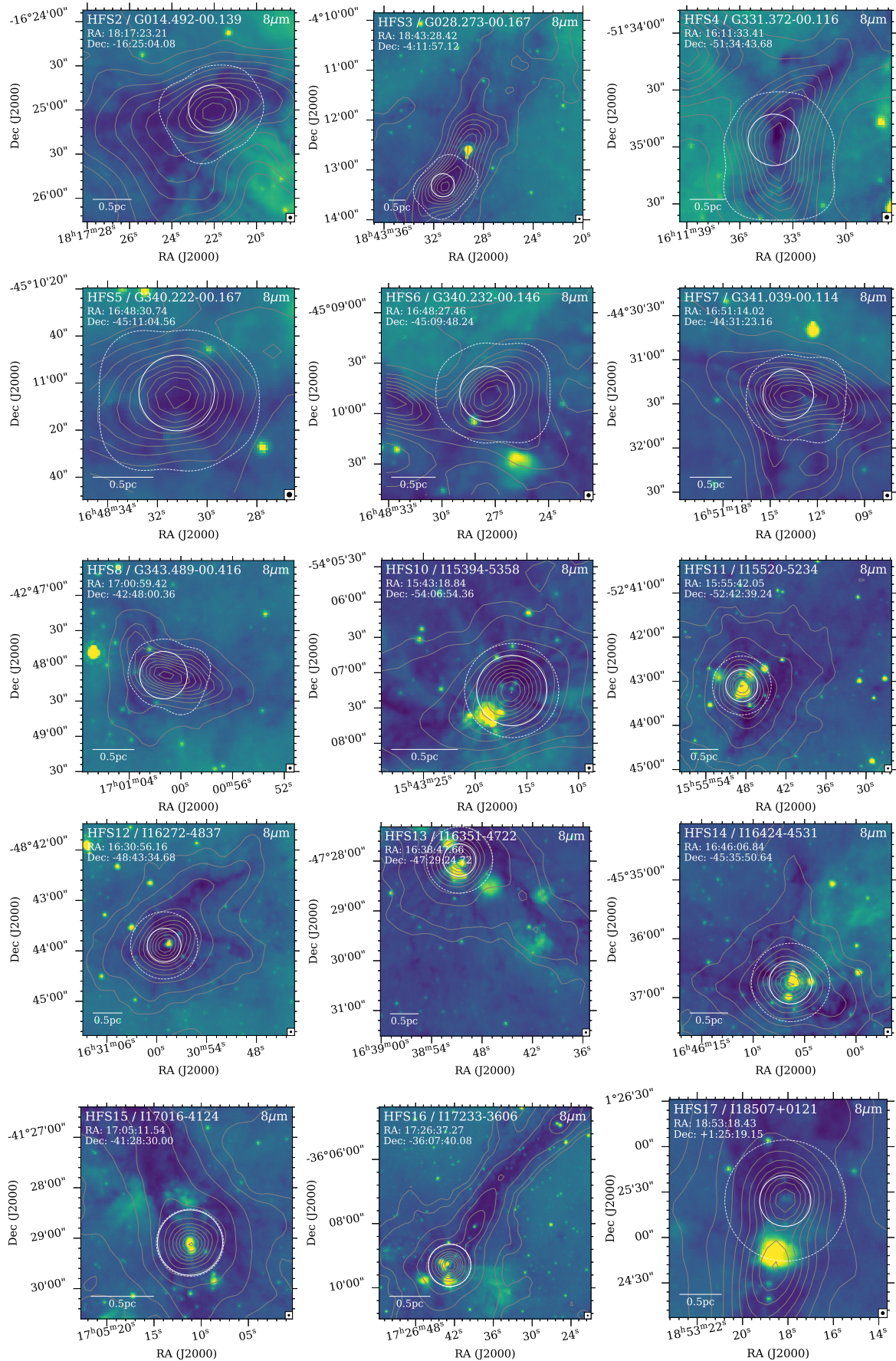


Figure A1. Same as Fig. 1 but for the remaining 15 HFSs.